CHARACTERIZATION OF SINGLE DEFECTS IN ZINC OXIDE

A Thesis

Presented to the Faculty of the Graduate School

of Cornell University

in Partial Fulfillment of the Requirements for the Degree of

Master of Science

by

Yun-Yi Pai

May 2014

ABSTRACT

This thesis summarizes my work on characterizing isolated defects in zinc oxide (ZnO). In chapter 1, I will briefly review the major strength of quantum information processing over classical computation. I will then review the basic properties of nitrogen-vacancy centers, the most-studied point defect species in diamond, and how they motivate the search for defects of similar properties in other semiconductor materials for defect-based quantum information processing. In chapter 2, I will describe our initial study on the optical properties of successfully isolated defects in ZnO: their fluorescence spectra, excited state lifetimes, and their photodynamics including blinking. In chapter 3, I will detail my work on extending the capability of an atomic force microscope to include simultaneous imaging in a confocal geometry. In chapter 4, I will discuss possible directions for our defect studies.

BIOGRAPHICAL SKETCH

Yun-Yi Pai was born on January 11, 1987 to Hsi-Ping Pai and Shu-Yueh Chi in Taipei, Taiwan. He attended Taipei Municipal Jianguo High School. Yun-Yi earned his Bachelor of Science degree in Physics at National Taiwan University in 2010. After completing his mandatory military service, he enrolled at Cornell University in the department of applied and engineering physics. He joined the Fuchs research group and studied isolated single defects in zinc oxide.

Dedicated to my parents, for their endless love and support.

ACKNOWLEDGEMENTS

First I would like to thank my advisor Gregory David Fuchs. He is the epitome of an experimental physicist: passionate, enthusiastic and extremely knowledgeable and keen to the realm of physics. He is also a wonderful advisor being both supportive and available while giving me the freedom to pace myself towards my thesis work. His guidance allowed me to gradually acquire the knowledge needed, reinforce my own passion for experimental physics and, equally importantly, further develop my physical intuition and scientific maturity. I deem myself lucky to have had the opportunity to be a member of the Fuchs research group.

I have been fortunate to work with many outstanding colleagues at Cornell University. In particular, I have received a great deal of encouragement and support from each member of the Fuchs research group. I learned much of the underlying theory and experimental nuances of single-molecule microscopy from Nicholas Ryan Jungwirth. I can still vividly remember the long nights that we worked painstakingly, in turns, to acquire antibunching and blinking power studies of isolated defects in zinc oxide nanoparticles and sputtered films. I also thank him for the informative discussions regarding my work on the confocal AFM setup and the samples we develop for EFM studies on our isolated defects.

I am also grateful to Evan Ronald MacQuarrie who generously fabricated samples for me at the CNF and always provide keen insights in our discussions. I thank Hung-Shen Chang for his well-controlled growth and characterization of our ZnO sputtered films. I thank Austin Moehle for discussions and various assistance including the design of the bracket for our cryostat and CNF fabrication. I would like to thank Jason Bartel for valuable discussions as well as monitoring our lab safety. I thank each member of the Fuchs research group for

their unwavering support and sincere friendship.

I would also like to thank David Muller for serving as my special committee member and for his helpful advice on my studies. I thank Christopher Henley for various assistances. Steve Kriske, who trained me on various tools at CCMR including the Asylum AFM and the 3-gun sputtering system, always assisted me when I needed help. I thank Deron at Asylum Research for helping me on the EDIM expansion module for Asylum ARC controller. I thank James ODea for sharing me his personal knowledge on the operation of ORCA AFM. I thank Cynthia Reynolds for administrative assistance. I thank Justin Rodriguez, Aniket Kakatkar, Andrew Chang, Yida Lin, Yin-Feng, Xue Bai, Zhe Wang, Gavrielle Rebecca Untracht, Fu Cheng, Ben Hoselton, Seth Hafferkamp, Justin Richmond- Decker for making my life in Ithaca a lot less stressful. I thank my roommate Chi-Feng Pai for being my mentor and beacon even before I applied for the program in applied physics at Cornell University.

Finally, I would like to thank my parents and my sister for their endless love and support.

TABLE OF CONTENTS

LIST OF TABLES

LIST OF FIGURES

CHAPTER 1

INTRODUCTION

Point defects in semiconductors have been studied for more than 50 years [1]. The field has attracted much attention recently, predominately led by the recent success in understanding and controlling isolated defects in semiconductor materials. The most important example is the nitrogen-vacancy (NV) center in diamond [2]. Various usage of these single defects have been realized such as sensing and bio-labeling [3–6]. Furthermore, the fact that these defects are stable source of single photons coupled to their spins —a quantum degree of freedom —makes them competitive candidates for the quantum communication and qubits, the unit for quantum information processing.

So why qubits, quantum information processing and quantum computers? A quantum computer encodes information in qubits. It stores, transmits, and processes information, basing on the laws of quantum mechanics. A quantum computer can exploit non-classical phenomena such as entanglement and superposition [7, 8]. This opens up a whole new avenue: there are problems computationally hard, or even impossible, to classical computers, but solvable to quantum computers. The most famous examples are factorization and database searching [9].

In 1996, Peter Shor discovered a quantum algorithm that exploits quantum entanglement and can solve the factorization problem in polynomial time, while classical computers can only solve in exponential time [10–12]. In 1998, L. K. Grover found a quantum algorithm that makes use of quantum superposition and can provide significant speedup in database searching [12, 13]. There are other notable algorithms such as Simons algorithm [14], Deutsch–Jozsa algo-

rithm are found exponentially faster than classical algorithms on the same problems [15]. The problems that are hard for a classical computer but solvable on a reasonable time scale by a quantum computer are believed to belong to a class of problems called non-deterministic polynomial-time (NP) intermediate problems [9]. The NP-intermediate problems, is a class of problems not in NP but not in P (solvable by classical computers) nor NP-complete (hardest in NP). Besides the aforementioned factorization problem and database search problem, other important examples are graph isomorphism, knot triviality, minimum circuit size problem, etc.

In addition to the computational power of a quantum computer over a classical counterpart, quantum information processing allows communications secure from eavesdroppers, based on the non-cloning theorem [16]. A quantum computer is also necessary for simulating quantum systems efficiently [17]. For example, simulating N spin-$\frac{1}{2}$ particles needs a classical computer to store 2^N coefficients, which scales up exponentially.

Before defect-based systems being adopted as experimental platform for quantum information processing, superconducting charge qubit [18] or flux qubit [19,20], cold ions/atoms qubits [21–24], and quantum dots qubits [25,26] have been realized. Various quantum controls including entanglement [22], and quantum error correction [23,27–32] have been demonstrated.

Isolated point defects in semiconductors, once regarded as unwanted accidents, turned out to be promising systems with an easily controllable quantum mechanical degree of freedom. They are likely to play pivotal roles in the realm of quantum information processing. Take NV centers for example, their spin states can function as the 2 states needed to form a qubit. They are also in-

trinsically sources of single photons, and they are stable at room temperature. Furthermore, it has also been shown that these single defects could be used as electric, magnetic [33,34], thermal sensors [5,6,35].

In this chapter, I will first review the most-studied semiconductor point defect, i.e., the NV center in diamond, and then how the defect studies led our attention to the isolated defects in zinc oxide (ZnO).

1.1 Nitrogen-Vacancy Center in Diamond

More than 500 defect species [36] have been reported in diamond. Among them is the negatively charged NV center (NV^-) in diamond, which is the most-studied point defect species. The spin state of this system can be addressed and readout optically at room temperature. Furthermore, it is among the earliest stable solid state sources of single photons at room temperature. They are robust. They have long spin coherence time. These features make NV centers appealing for the sensing such as magnetometry, and also an appealing platform for experimental quantum information processing.

Structure, Optical Properties and Spins of NV Centers

Structurally the negatively charged NV center is a substitutional nitrogen atom adjacent to a carbon vacancy. Nitrogen is the most abundant impurities in diamond and can occupy up to 1% of the total mass. The additional electron pair forms a S=1 electronic spin in the system. There are two other charge states for the NV centers: NV^+ and NV^0, but neither of them has spin-dependent fluores-

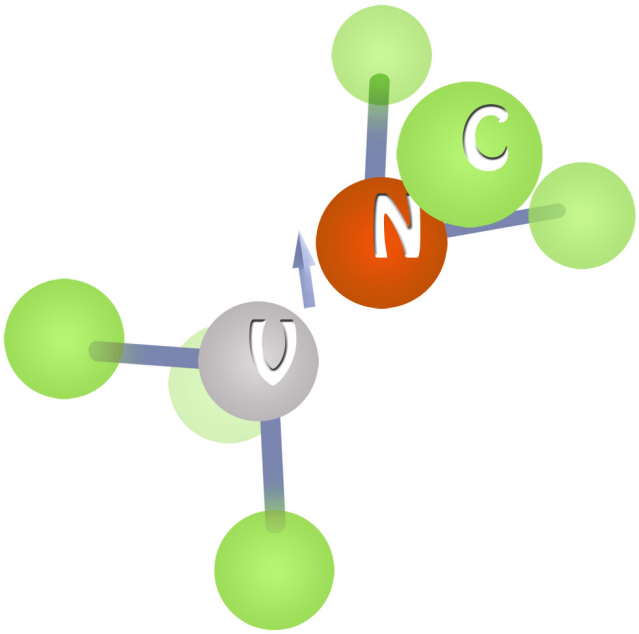

Figure 1.1: Structurally the negatively charged NV center is a substitutional nitrogen atom adjacent to a carbon vacancy with an additional electron captured from the bulk.

cence contrast. I will abbreviate NV^- to NV from now on.

The vacancy is tetrahedrally coordinated. The overall system has C_{3v} point group symmetry. Its irreducible representation gives $C_{3v} = A_1 \oplus A_2 \oplus E$, 2 orbital singlets and a doublet. The doublet suffers from dynamic Jahn-Teller narrowing [37], that is, the phonon-assisted relaxation between the doublet levels. The doublet can be resolved at cryogenic temperatures ($\lesssim$20 K).

The ground state of the system is identified as a spin triplet $^3A_2$. It has a long shelving state involving $^1A_1$ and ^1E. The spin sub-levels split due to the alignment of the two electronic spins, the zero field splitting, and transition between sub-levels can be mediated by RF pulses.

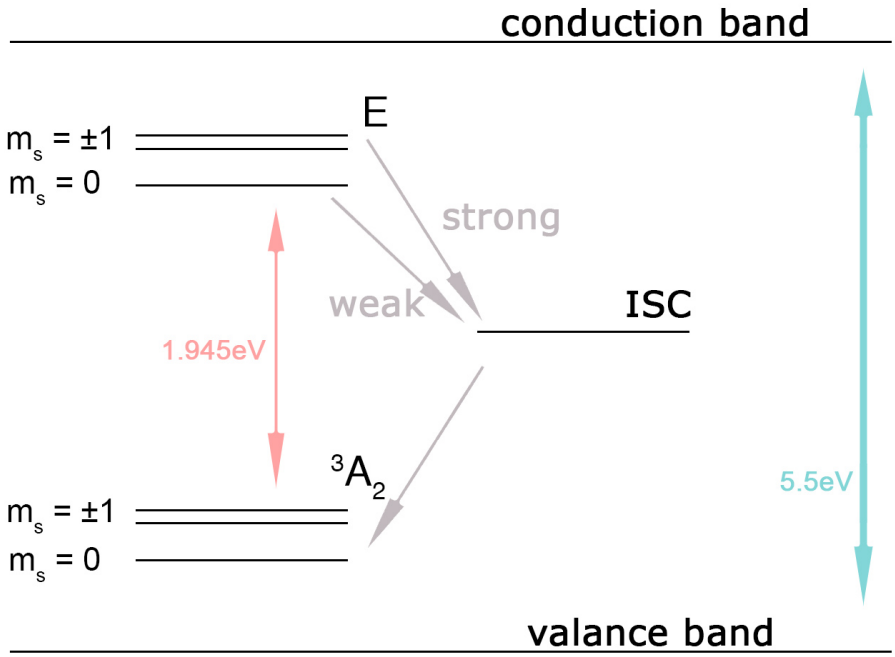

Figure 1.2: Energy level of an NV^- center. The size of the bandgap is 5.5 eV. The negatively charged state gives the system overall electronic spin 1 and the ground state of the system is identified as a spin triplet $^3A_2$. The long shelving state involves $^1A_1$ and ^1E. The energy difference between the excited state and the ground state is 1.945 eV. The $m_s = \pm 1$ levels have higher energy due to the zero field splitting. Note that the splitting magnitude for the ground state triplet and the excited state triplet are different.

The direct transitions between $^3A_2$ and ^3E is 637 nm, known as the zero phonon line (ZPL) of the NV. This transition is spin-conserving. The transition between $^3A_2$ and its long shelving states is non-radiative and spin-selective. The coupling of the $m_s = 0$ sublevels to the long shelving state is weaker. Therefore the photoluminescent intensity is spin-state dependent. By simply pumping the NV center to its excited state, the $m_s = 0$ spin state of the system will be popu-

lated. Also, because of the long shelving states, the photoluminescence of NV is stronger when it is in $m_s = 0$ initially, therefore the spin state of NV can be measured optically.

The coherence time of the electronic spin of the NV centers has achieved 100 μs for free induction decay, milliseconds for Hahn echo at room temperature [38], and ~0.6 seconds for dynamic decoupling sequence at 77K [39]. Coupling between the electronic spin of an NV and the nearby isolated nuclear spins, such as nitrogen atom or ^{13}C, has been demonstrated. The electronic spin can be used as a register to control and detect long lived nuclear spins nearby [40].

Recent Works and Limitations of NV Centers

As a source of single photons, it is stable and hard to be destroyed optically. At room temperature it emits in ZPL with a broad phonon side band at around 630 nm to 800 nm. However, quantum cryptography using NV centers as single photon sources for BB84 (the first quantum key distribution protocal developed by Charles Bennett and Gilles Brassard in 1984) is still possible [41]. As a qubit candidate, the properties of individual defects are affected by their environment. Typical diamond has relatively large variation in crystal strain, hence the defects are intrinsically non-identical. However, external perturbations such as electric fields can tune the NV centers to make them identical, making them ready for entanglement [42]. Entangling NV centers that are several meters away from each other has been demonstrated [43]. As a sensor, incorporating single NV center to probes such as AFM cantilevers can sense the local field in the vicinity of the sample [3].

The most spatially controlled method of creating NV centers in diamond is through ion implantation. Although the NV centers are ideal for quantum information processing, their diamond host is hard to engineer compared to conventional semiconductor materials. This limits the scalability and potential of the NV centers significantly because diamond has minimal epitaxial compatibility with other materials. The growth and fabrication methods of diamond are also very limited compared to conventional semiconductor materials. These limitations of diamond have motivated the search of the NV-like point defects in conventional semiconductors like ZnO. The control of defects in silicon carbide (SiC) has also been demonstrated recently.

Other Defects in Semiconductor Materials

The search of NV-like defects in more conventional, technologically mature semiconductor materials could lead to designs unaccessible for NV centers in diamond. Weber *et. al.* have listed several criterion for host materials and for defect centers to be candidates for qubits. Candidates that have been studied recently for the search of NV-like defects include silicon carbide (SiC) divacancy ($V_{Si}V_C$) in SiC [44,45], $V_{Al}O_N$ in aluminum nitride [46], $V_{Ga}O_N$ in gallium nitride (GaN) [47]. Recently, Morfa *et al.* reported isolated defects in ZnO and assigned the red emissions of the isolated defects to zinc vacancy V_{Zn} [48].

1.2 Zinc Oxide

ZnO is a relatively conventional material in semiconductor industry [49–51]. It is technologically mature. ZnO has many growing methods available [52],

from chemical vapor deposition, laser ablation [53], pulsed laser deposition, arc discharge, molecular beam epitaxy (MBE) [54]. It can be grown into high quality single crystals and many nanostructure forms such as nanorods, pillars or tubes.

ZnO is a wide-bandgap II-VI semiconductor, with direct band gap 3.3 eV at room temperature. It has high electron mobility [55, 56] and transparency [57], which can be controlled by the doping level. Because of these characteristics, it has been used in transparent electrodes [58], piezoelectric resonators [59], light emitting diodes [60], photovoltaic applications [61]. It has also been used in varistors for its highly nonlinear current-voltage curve [62]. It has large heat capacity, high thermal conductivity and low thermal expansion, which makes ZnO appealing in ceramic productions.

The structure of the ZnO crystal is usually wurtzite or zincblende. Piezoelectricity presents in both wurtzite and zincblende while pyroelectricity is only observed in wurtzite structure. Point defects in ZnO wurtzite has C_{3v} point group symmetry.

The previous defects studies in ZnO [63–70] include photoluminescence, electric paramagnetic resonance, magnetic resonance, observation of isolated single defects is also reported, but most of those studies are ensembles. Therefore, different defect species, with different intrinsic properties could be averaged together, while their single-defect dynamics remain hidden and broaden the observed spectra. Isolated defects in nanoparticle film have been reported [48].

Ensemble observation may also obscure the dependence of the properties of the single defects on their local environment. Using the techniques in single-

molecule microscopy, we study the defects in ZnO, one at a time, and therefore probe the distinct properties of each defect. In the next section, I will describes the optical properties of isolated defects, including fluorescence lifetime, spectrum, and the random discrete jumps between different photoluminescence intensities, which is often referred as *blinking*.

CHAPTER 2

SINGLE DEFECTS IN ZINC OXIDE

In this chapter I will review the experimental techniques, optical properties of the single defects that we have observed in our ZnO samples. This includes description of the experimental setup, the measurements of second-order correlation function of photon arrival times, fluorescence spectra and the blinking behavior of the defects. The details of our samples for are included at the end of this chapter, together with the 19 relevant isolated defects. This work is also described in [71].

2.1 Confocal Microscopy and Photon Antibunching

To address the single defects in our samples, we use a standard confocal microscopy with Hanbury—Brown and Twiss setup. We use a 532 nm (2.33 eV) green laser to provide sub-bandgap (3.3 eV) excitation in ZnO. The beam is focused by a microscope objective. Sample imaging is done by a fast scanning mirror (FSM). The emission, which has lower energy than the excitation, due to phonon coupling, collected by the same objective, goes through a path different from the excitation path (because of a dichroic mirror). The emission then enters a Hanbury—Brown and Twiss setup. The Hanbury—Brown and Twiss setup has a 50:50 beam splitter, two avalanched photodiodes (APD) for detecting the emission, and time correlated single photon counting (TCSPC) module (Becker & Hickl, SPC-130).

We measured the second order correlation function $g^{(2)}(\tau)$ to verify that the

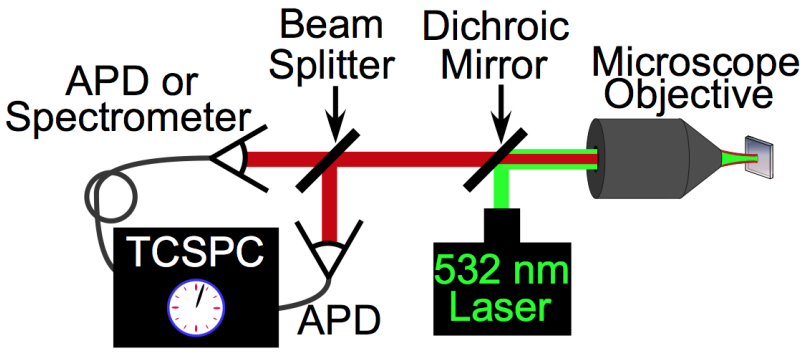

Figure 2.1: Schematics of confocal with Hanbury-Brown and Twiss setup. A 532 nm laser is employed to provide sub-bandgap excitations. The photoluminescence after the excitation is then collected and correlated by a time correlated single photon counting (TCSPC) module in the Hanbury-Brown and Twiss setup.

addressed emitter is isolated and not an ensemble [72]:

$$g^{(2)}(\tau) = \frac{p_e(\tau|0)}{p_e^{st}} \tag{2.1}$$

where $p_e(\tau|0)$ is the conditional probability for emitting a photon at time τ, given that it has emitted a photon at time t = 0, and $p_e^{st} = p_e(\pm\infty|0)$ is the steady state probability of emitting a photon. We modelled the observed photoluminescence by a single-photon process: a defect goes to its excited state by absorbing a photon, and by emitting a photon it returns to its ground state. We assume that the time required for it to be re-excited and then emit another photon is not infinitesimal. Therefore, for an ideal emitter that can emit only one photon at a time, its second order correlation function should satisfy $g^{(2)}(0) = 0$ and $g^{(2)}(\pm\infty) = 1$ (normalization of photoluminesce intensity in steady state [73]). The dip, $g^{(2)}(0) < g^{(2)}(\pm\infty)$ is referred as *antibunching*, a manifestation of sub-Poissonian statistics, permitted only in nonclassical sources.

Experimental non-idealities such as detector dark counts, jitter, nonlinear-

ity and finite resolution, as well as uncontrolled reflections at various optical elements, would contribute the counts at $g^{(2)}(0)$. However, the $g^{(2)}(\tau)$ for two equally powered, identical emitters at time $\tau = 0$ can only go to 0.5 [74]. It is therefore a standard practice to use $g^{(2)}(0) < 0.5$ as the criterion for whether we are addressing an isolated defect or not. However, an antibunching dip $g^{(2)}(0) < 0.5$ is still possible for non-identical emitters having different intensity levels or intermittent photoluminescence.

Here figure 2.2 shows 2 sets of antibunching curves, taken from two different defects at three different excitation powers. The *bunching*, referring to the value higher than the asymptotic value, i.e., $g^{(2)}(\tau) > g^{(2)}(\pm\infty)$, is apparent in second set of curves when being excited by higher laser power. This is an indication of that there are at least three pertinent states in the transition.

2.2 Sample Details

The samples we studied include both ZnO nanoparticles and ZnO sputtered films. The nanoparticles were purchased from Sigma Aldrich. The nanoparticle sample were by dropcasting onto fused silica substrates. The nanoparticles were suspended in methanol before dropcasting.

We have observed antibunching in undoped nanoparticle samples. The XRD indicates that our nanoparticle sample has wurtzite structure with mean particle size 75 nm.

The thin ZnO film, both doped and undoped, are grown by DC reactive sputtering at room temperature. The argon (4 mTorr) was introduced after the

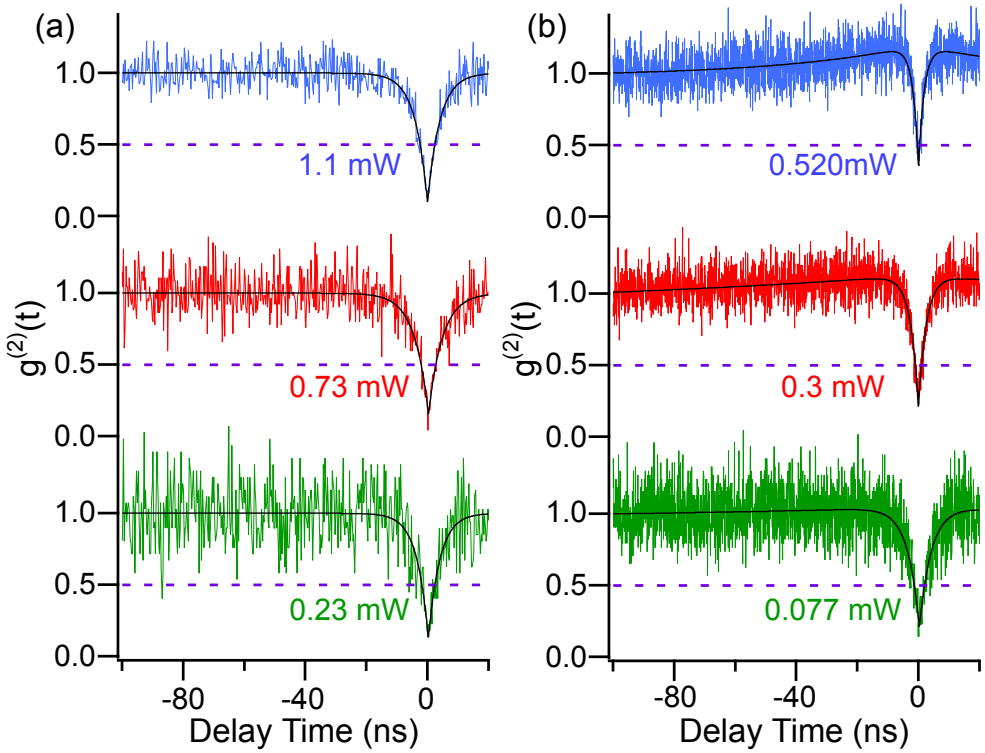

Figure 2.2: 2 sets of antibunching curves.

chamber was pumped to base pressure 5×10^{-7} Torr. Then the oxygen is also introduced, with partial pressure 1 mTorr. The film thickness is measured by contact profilometry, yielding 72.5 nm for the undoped sputtered film sample. XRD study indicates the film is (002) oriented, with mean grain size 50 nm. The Al-doped ZnO sputtered film was grown by co-sputtering an aluminum oxide target. For Al-doped sputtered film, we have observed 6 emitters with $g^{(2)}(0) \sim 0.5$, one of which changed from 2-level blinking to 3-level blinking during the observation, but we have not seen any $g^{(2)}(0)$ well below 0.4.

All the samples are air annealed after desposition, on a hotplate set at 500°C, for 30 mins. We have not seen any isolated emitters in our samples before annealing.

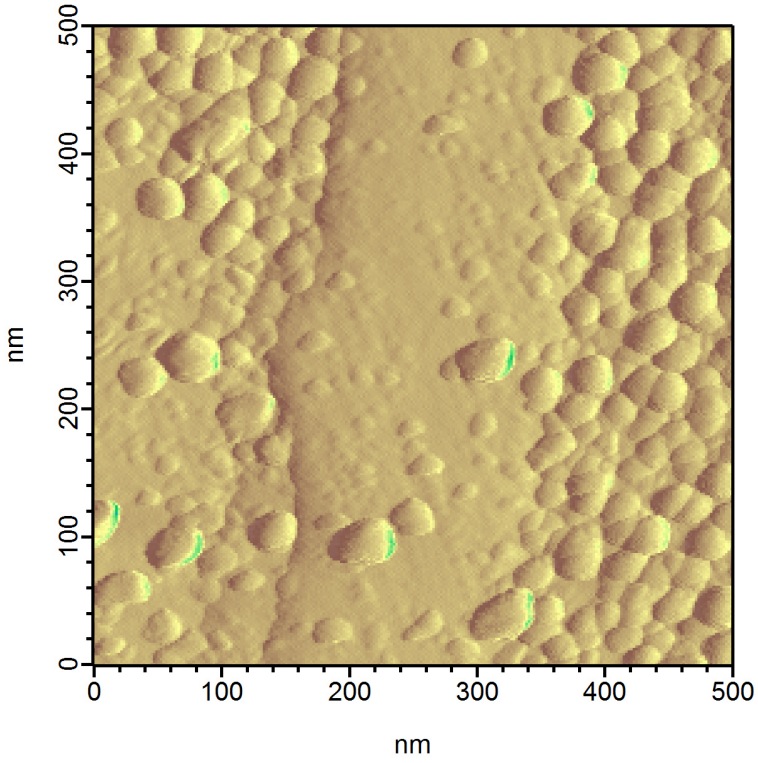

Figure 2.3: An AFM image of an undoped ZnO sputtered film sample. The thickness of the deposition is 72.5 nm. The image was taken by Hung-Shen Chang in our group.

2.3 3-State Model

To analyze the $g^{(2)}(\tau)$ measured for the isolated defects in our samples, we relate the emission of the defects to 3-state model, with a ground state $|1\rangle$, excited state $|2\rangle$, and a metastable shelving state $|3\rangle$. Figure 2.4 shows 3 possible scenarios. The excited state of the leftmost scenario is in the conduction band; the ground state of the right most scenario is in the valence band. These are the three simplest scenarios consistent with our observations. We assume that the transition from the ground state to the excited state requires the absorption of a photon, and the system emits a photon to relax directly from the exited state to

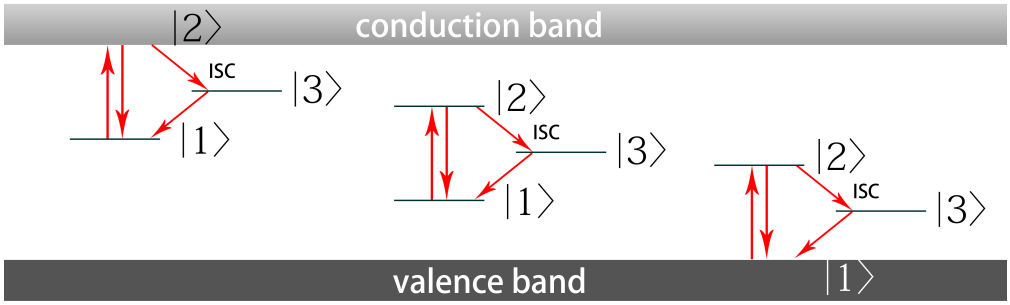

Figure 2.4: Level Diagram

the ground state. The system can also undergo a non-radiative process, relaxing from the excited state to the third state, then the ground state.

It has been reported that a weakly coupled third state suggests that the transition is spin-mediated [75–77]: the third state usually possess different spin projection from the spin projection of the other two states, hence the transition rate between the ground state and the third state, and the rate between the excited state and the third state, are lower because the spin projection is modified during the transition.

The rate model describing this 3-level system can be written as [78]:

$$\frac{d}{dt}\begin{pmatrix} P_{|1\rangle} \\ P_{|2\rangle} \\ P_{|3\rangle} \end{pmatrix} = \begin{pmatrix} -r_{12} & r_{21} & r_{31} \\ r_{12} & -r_{21}-r_{23} & 0 \\ 0 & r_{23} & -r_{31} \end{pmatrix} \begin{pmatrix} P_{|1\rangle} \\ P_{|2\rangle} \\ P_{|3\rangle} \end{pmatrix} \tag{2.2}$$

where $P_{|i\rangle}$ is the probability of the system in state $|i\rangle$, and r_{ij} is the rate of the transition from state $|i\rangle$ to state $|j\rangle$. For this rate model we have ignored the time dependence of the rates. The second order correlation function is proportional to $p_e(\tau|0)$, the conditional probability for emitting a photon at time τ, given that it has emitted a photon at time t = 0. The initial condition satisfying these is $P_{|1\rangle}(0) = 1$, $P_{|2\rangle}(0) = 0$, $P_{|3\rangle}(0) = 0$ [78]. The conditional probability for emitting a

photon at time τ is proportional to $P_{|2\rangle}$, i.e., the probability of the system being in the excited state. After normalization, the second order correlation function can be expressed as:

$$g^{(2)}(\tau) = 1 + Ae^{\lambda_1|\tau|} - (1 + A)e^{\lambda_2|\tau|} \tag{2.3}$$

where A is determined by the transition rates, the λ_1, λ_2 are two negative eigenvalues of the transition rate matrix. Note that bunching, which is referring to $g^{(2)}(\tau) > 1$, for some time τ, is not possible in a 2-level model. A solution for the expression of $g^{(2)}(\tau)$ in a 2-level model will only allow one exponential term, which eliminates the possibility of bunching.

The excited state lifetime $\tau_{|2\rangle} = \frac{1}{r_{21}+r_{23}}$ can be obtained either directly measuring time-resolved fluorescence with a by pulsed laser excitation or by fitting the second order correlation $g^{(2)}(\tau)$ 3-state model. The pulsed laser excitation is not able to decouple the two rates and extract the lifetime of the third state $\tau_{|3\rangle}$. By solving the 3-state model analytically, we obtain an expression of the second order correlation function $g^{(2)}(\tau)$ similar to the one listed above, not in terms of λ_1, λ_2, but the in terms of the transition rates r_{ij}. We extract the individual rate by fitting the correlation of the photon arrival times acquired from the emitter being excited by the laser to the analytical expression of $g^{(2)}(\tau)$. For each defect, we acquired its second order correlation of photon arrival times at several excitation power levels, then fit this family of curves with a single analytic expression for $g^{(2)}(\tau)$ and allow the excitation rate r_{12} to depend on the excitation power linearly, while holding all the other rates r_{ij} constants the same for the same defect. The fitting is done by standard chi-squared minimization. The minimum of chi-square is more sensitive to the lifetime of the excited state $\tau_{|2\rangle}$ and less sensitive to the lifetime of the third state $\tau_{|3\rangle}$.

For the first set of curves in figure 2.2 ,we obtained $\tau_{|2\rangle} = 4.8 \pm 0.2$ns, consistent with $\tau_{|2\rangle} = 4.5 \pm 0.3$ns from pulsed laser measurements. For the 19 defects that we have seen with $g^{(2)}(0) < 0.4$, $\tau_{|2\rangle} = 1.7 - 13$ns, $\tau_{|3\rangle} = 40 - 300$ns. The lifetimes of the 19 defects are listed in table 2.1. The inverse of the lifetimes of the excited state, $\frac{1}{\tau_{|2\rangle}}$, are plotted as figure 2.5. Additionally, we have seen 6 emitters that exhibit sub-Poissoninan photon emissions in the Al-doped sputtered film sample, but all of their $g^{(2)}(0)$ are only around 0.5 and none of them go well below 0.4, the criterion we used.

A critial question is: does the 3-level system involve the conduction band? That is, is the leftmost scenario in figure 2.4 the case? We expect, for conduction band transitions, $\frac{1}{\tau_{|2\rangle}} = nC_n$, with local carrier concentration n and electron capture coefficient C_n. Although we have not characterized the carrier concentration of our samples, we expect the carrier concentration is higher in the Al-doped samples, compared to undoped samples. We have not seen single defects with $g^{(2)}(0) < 0.4$ in Al-doped sputtered film sample, therefore comparison between doped and undoped sputtered film samples is insufficient. Furthermore, ZnO films may depend on the growth details, and individual defect may depend on the grain size, geometry, surface chemistry, their local fields and strain. Additionally, the Al dopant may introduce different structure, modify the size of the bandgap, defect concentration.

For the defects in nanoparticle sample, the wider distribution of the $\frac{1}{\tau_{|2\rangle}}$ might be due to the size, geometry and surface chemistry of the nanoparticles. As an example, in the case of nanodiamonds, the excited state lifetimes of NV centers depends on the particle size, because additional non-radiative relaxation channels are more favorable in nanodiamonds. Similar mechanisms might play an

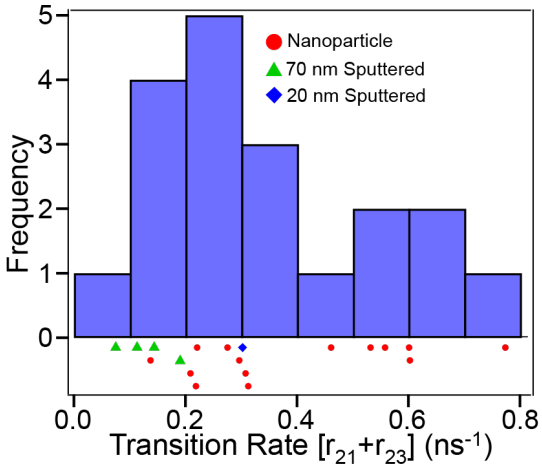

Figure 2.5: Histogram of inverse of the lifetimes of the excited state, $\frac{1}{\tau_{|2\rangle}}$ of the 19 defects in our samples that has $g^{(2)}(0) < 0.4$.

important role in the excited state lifetimes of defects in ZnO nanoparticles.

2.4 Fluorescence Spectra

Examples of emission spectra from isolated defects in our ZnO samples are displayed in figure 2.6. Each of the spectra is normalized. The dash line around 580 nm indicates the filter edge from the long pass filter (Omega Optical, 3rd Millennium 560nm Long Pass Filter).

All of the spectra that we acquired and summarized in table 2.1 feature two Gaussian peaks. Each of the two peaks are from the emission of an isolated defect being excited, not from the background or other defect nearby. Eight of them have peaks separation around 150 meV. The positions of the lower peaks are around 1.82 to 1.97 eV, while the higher peaks are within 1.91 to 2.08 eV. These characteristics are consistent with prior work [48] with the peaks in this

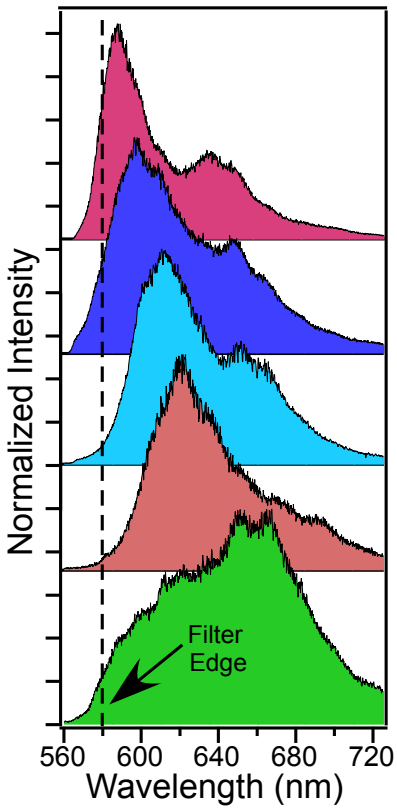

Figure 2.6: Examples of emission spectra from isolated defects in our ZnO samples. Each of the spectra is normalized. The dash line around 580 nm indicates the filter edge from the long pass filter (Omega Optical, 3rd Millennium 560nm Long Pass Filter).

work are slightly more energetic.

2.5 Photodynamics and Blinking

Instabilities, random intermittency of the photoluminescence intensity, or blinking, are nearly universal to single emitters and have been observed in all known types of fluorophore so far, including single molecules, quantum dots, fluorescent proteins, and semiconductor nano-structures. Sometimes the photolumi-

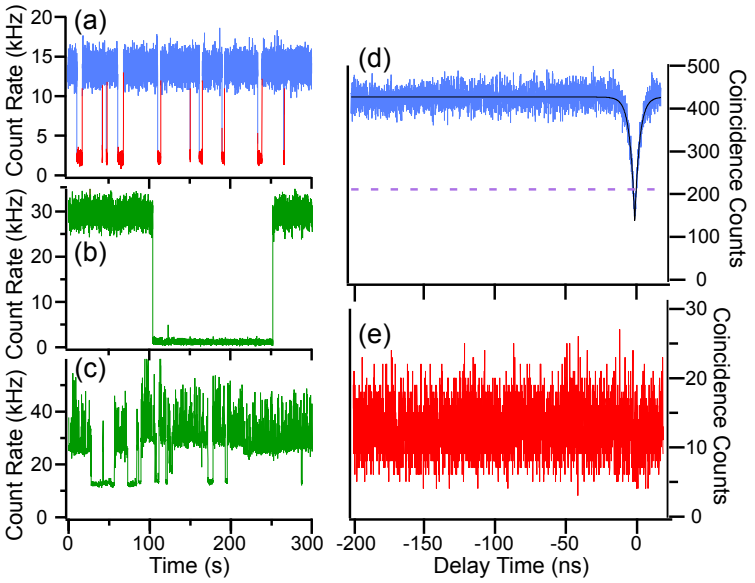

Figure 2.7: Parsed antibunching curves for the bright and dark state. Figure (a) and (b) are from the defect 3 and defect 4 listed in the table 2.1, respectively. Figure (c) shows a more irregular behavior. Figure (d) and (e) are the $g^{(2)}(\tau)$ for the bright state and the dark state of defect 3. The antibunching is prominent in the $g^{(2)}(\tau)$ for the bright state, while the $g^{(2)}(\tau)$ for the dark state indicates the arrival times for the dark state is uncorrelated. Therefore, the defect is inactive or emitting at wavelengths that are not detectable by our setup.

nescence intensity has distinct discretized states of photoluminescence intensity levels. The observed dwell times for the distinct states of intensity typically follow either a power law or an exponential distribution. The instabilities of the photoluminescence intensity may result from the changes of the environment [79, 80], spectral diffusion [81, 82], the system entering a long-lived metastable state [80, 83, 84], or a charge state instabilities [85]. The behavior might change with applied external magnetic, electric field or stress and therefore potentially could be used as a sensor [86].

Instabilities of the photoluminescence intensity in isolated defects in ZnO

have also been observed. Most of the isolated defects in our samples have stable photoluminescence intensities under multiple time binning resolutions. However, some of the defects are switching between distinct 2 or 3 levels of intensity. Still some of them exhibit complicated multi-state dynamics.

For the 19 defect listed in table 2.1, 6 defects have discrete levels of intensity. Figure 2.7 shows three examples of blinking between bright and dark states. Figure 2.7 (a) and (b) are from the defect 3 and defect 4 listed in table 1, respectively. Figure 2.7 (c) shows a more irregular behavior. Figure 2.7 (d) and (e) are the $g^{(2)}(\tau)$ for the bright state and the dark state of defect 3. The antibunching is prominent in the $g^{(2)}(\tau)$ for the bright state, while the $g^{(2)}(\tau)$ for the dark state indicates the arrival times for the dark state is uncorrelated. Therefore, the defect is inactive or emitting at wavelengths that are not detectable by our setup.

Defect 5 exhibits more complicated dynamics. Figure 2.8 is a 500-second photoluminescence intensity versus time capture for defect 5. It exhibits both a fast blinking dynamics, with dwell times on the order of several milliseconds, that spans, for example, the first 150 seconds of the capture, and interrupted by a longer inactive states with dwell times on the order of tens of seconds.

We studied the dwell times of the bright states and the dark state of defect 3 and defect 5, and their power dependence. Careful binning is necessary for resolving the faster dynamics and avoiding artifacts. The intensity data is then parsed into bright or dark states by a threshold. Both the dwell times for the bright state and the dark state follow an exponential distribution.

We measured the rate for leaving the bright state $1/\langle\tau_{BS}\rangle$ and rate for leaving the dark state $1/\langle\tau_{DS}\rangle$. For defect 3, we observed that both $1/\langle\tau_{BS}\rangle$ (figure 2.8 (e))

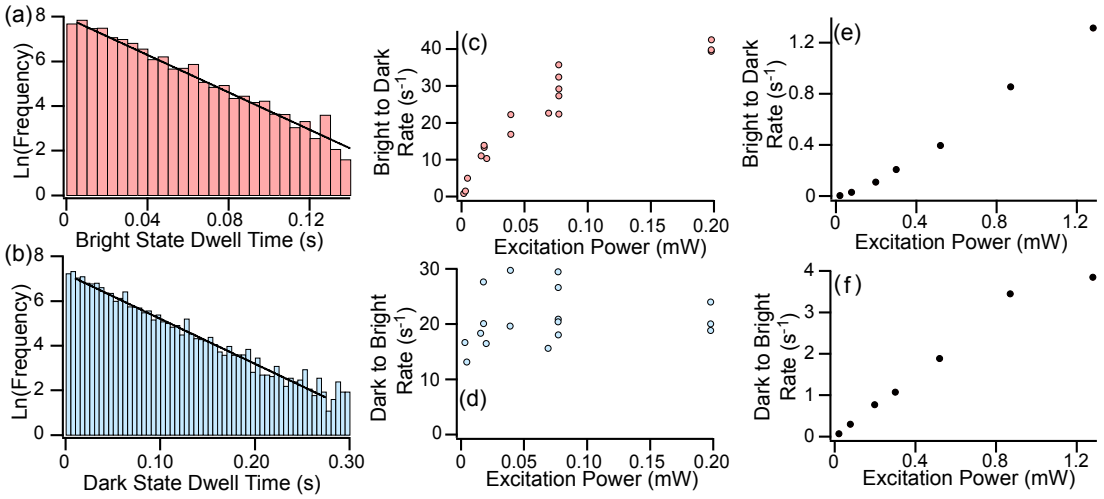

Figure 2.8: Dwell times.

and $1/\langle\tau_{DS}\rangle$ (figure 2.8 (f)) increase as the excitation power, while for defect 5, $1/\langle\tau_{DS}\rangle$ (figure 2.8 (d)) seems to be uncorrelated.

For defect 5, the fact that $1/\langle\tau_{DS}\rangle$ is uncorrelated with excitation power while $1/\langle\tau_{BS}\rangle$ does, indicates that the bright state is more energetically favorable. The blinking statistics are consistent with a metastable state with $\tau_{|3\rangle}$ =50 ms. This could indicate that the dark state is coupled to the metastable state, and a transition from the bright state to the dark state could correspond to a transition from $|2\rangle$ to $|3\rangle$. If the 3-state system is coupled to the conduction band, thermally or optically, with the $|2\rangle$ state in the conduction band, a transition from the bright state to the dark state would be an instance of ionization; furthermore, the bright state has favorable charge state as opposed to the dark state.

Defect 3, on the other hand, seems to be governed by a different mechanism. Both $1/\langle\tau_{BS}\rangle$ and $1/\langle\tau_{DS}\rangle$ increase with the excitation power, hence a simply band-assisted mechanism is less likely to be the case. A possible scenario

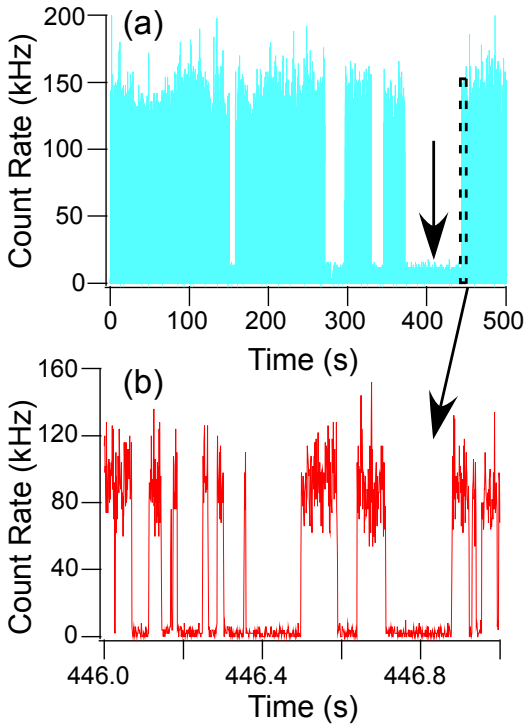

Figure 2.9: Photoluminescent intensity versus time of the defect 5, a 500-sec capture. The dynamics involve faster blinking between the bright and dark state with millisecond scale lifetimes, the first 150 seconds, for example; and jumps between fast blinking and inactive state of lifetimes longer than 10 seconds. For the fast blinking state, the bright state and the dark state are parsed and the histogram of the dwell times are plotted as figure 2.8.

that explains the blinking statistics of defect 3 could be a near by charge acceptor, such as a surface trap of the charge. A blinking event then is a transfer of the charge between the defect and the acceptor. The acceptor captures the charge and the defect jumps to its dark state.

Due to the insufficiency of relevant observations, it is not possible to determine the mechanism regulating the blinking behavior in these defects. The differences in qualitative nature of the blinking behavior of defect 3 and defect 5 suggest different species of dark state. Furthermore, a single defect could cou-

Defect	Sample	$\tau_{\|2\rangle}$	$\tau_{\|3\rangle}$	Spectral Peaks (eV)	Separation (meV)	Intensity
1	nanoparticle	4.8± 0.2		(1.91,2.04)	130	Stable
2	nanoparticle	3.2± 0.1	52± 5			Fluctuates
3	nanoparticle	4.53± 0.03				On/Off
4	nanoparticle	2.17±0.03	280±200	(1.88,2.06)	180	On/Off
5	nanoparticle	1.66±0.03		(1.94,2.08)	340	On/Off
6	nanoparticle	1.29±0.05		(1.94,2.07)	130	On/Off
7	nanoparticle	3.37±0.04				On/Off
8	nanoparticle	1.92±0.03	Unknown			Stable
9	nanoparticle	1.79 ±0.04	100±15	(1.93,2.08)	150	Stable
10	nanoparticle	1.66±0.04	44±2			Fluctuates
11	nanoparticle	4.6 ± 0.2	100±20	(1.97,2.11)	140	Fluctuates
12	nanoparticle	3.25±0.03	221±5	(1.89,2.03)	140	Fluctuates
13	nanoparticle	3.6±0.3				Fluctuates
14	nanoparticle	7.3±0.2		(1.89,2.06)	170	Fluctuates
15	20 nm sputtered film	3.3±0.1		(1.95,2.08)	130	On/Off
16	71 nm sputtered film	5.2±0.3				Fluctuates
17	71 nm sputtered film	13.4±0.6				Fluctuates
18	71 nm sputtered film	8.8±0.2	Unknown			Fluctuates
19	71 nm sputtered film	6.9±0.03		(1.82,1.91)	90	Fluctuates

Table 2.1: List of the 19 successfully isolated defects with $g^{(2)}(\tau) < 0.4$.

pled to more than a dark state specie, and defect 3 itself could be an example. There are at least two mechanisms regulating the blinking of defect 3, one is characterized by rapid jumps between bright and dark states with dwell times on the order of several milliseconds, the other is with dwell times on the order of 10 seconds. The later is unlikely to be an instance of the distribution of the former, for the dwell times are differ by 4 orders of magnitude and the statical probability is only approximately $10^{-85}\%$. In fact, dark state with dwell time longer than minute for defect 5 has been observed. The statistic observation for the longer blinking is not enough for characterizing the mean transition rate, however, it is apparent that defect 5 is coupled to 2 distinct mechanisms. Furthermore, all of the defects that we have seen went into a much longer inactive dark state, at least on the order of 10 mins. Our observation of each defect is terminated by this event.

CHAPTER 3

CONFOCAL-AFM

Combining confocal and atomic force microscopy (AFM) allows the strengths of each technique to be used together. The strengths of the confocal microscopy include time correlated single photon counting, and several super-resolution techniques that bypass the Abbe diffraction limit developed [87–89] recently, including the stimulated emission depletion (STED). AFM, besides its potential for atomic resolution [90, 91], has various other uses. These include conductive or tunneling AFM, scanning voltage microscopy [92, 93], electric field or charge sensing [94], and magnetic force microscope (MFM) [95]. Furthermore, tips made out of a high-purity diamond nanopillar with a carefully placed NV center near the end of the tip has also been fabricated [3, 96]. Therefore, the NV center can be brought much closer to the sample, increasing the overall sensitivity significantly as a nanosensor. The AFM tip can also be used to cause intentional damage, such as nanoshaving, nanografting [97] and local oxidation nanolithography (LON) [98]. The integration of confocal microscopy and AFM has been increasingly popular recently [99], including combined STED and AFM [100, 101].

With the abilities of controlling tip position accurately and reliably, it is possible to monitor the interaction between the sample, or isolated defects in our case, and the tip by photoluminescence intensity as a function of tip position, applied field strength, etc. A Hanbury-Brown and Twiss setup may also be used for monitoring the lifetimes $\tau_{|i\rangle}$ for each state. For our study, a confocal setup can address isolated defects optically, and an aligned AFM setup can provide additional local topographical information for the defects. This is necessary in

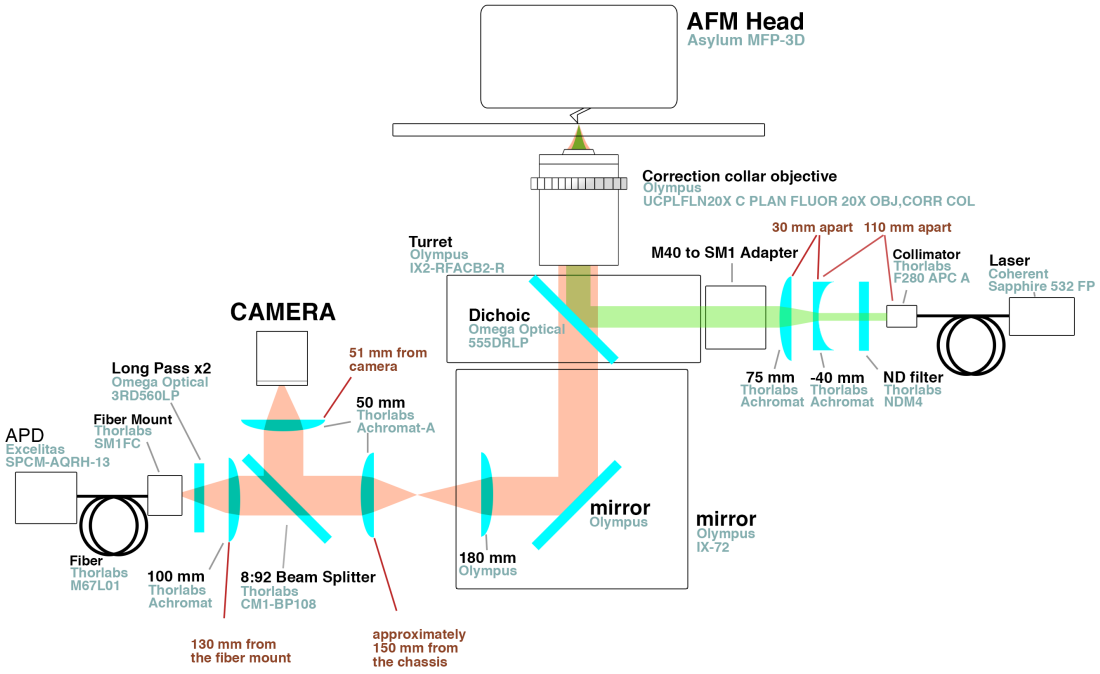

Figure 3.1: Schematics of our confocal-AFM setup. A home-built confocal microscope is added to a commercial AFM (Asylum Research, MFP3D-Bio-AFM-SPM). The 532 nm excitation beam is collimated, then focused by an microscope objective and illuminates the sample from beneath. The emissions from the sample are then collected by the same objective, and finally reaches the APD.

separating the intrinsic properties of the defects from the affects due to it surroundings, such as local strain, grain boundaries.

3.1 Schematic Diagram and Components

We now turn to the design and assembly of a home made confocal microscope added onto a commercial AFM (Asylum-MFP3D-Bio-AFM-SPM) at Cor-

nell Center for Material Research (CCMR). The AFM head is mounted onto the chassis of an inverted optical microscope (Olympus IX-71). The alignment is done with the magnification of the chassis set to 1.7x. Here the AFM head and the sample can be positioned separately, so that the tip and the focus of the confocal setup can be aligned. The goal of the setup is to perform simultaneous acquisition of AFM and confocal images. This setup will then also be compatible with the built-in capabilities of the AFM model such as electrostatic force microscopy (EFM), Kelvin probe microscopy (KPM), magnetic force microscopy (MFM), conductive-AFM (ORCA).

We use fiber-pigtailed semiconductor laser (Coherent, Sapphire 532 FP, λ = 532 nm) to provide sub-bandgap excitations for our intended sample ZnO. The laser beam goes through a collimator (Thorlabs, F280 APC A, on an AD11-F holder) and an expansion lens pair (Thorlabs, f=-40 and f = 75 achromats) and neutral density filter (Thorlabs, NDM4). To incorporate the excitation beam path into the chassis, a non-standard turret unit (Olympus, IX2-RFACB2-R) is used. An extruding piece of the chassis was filed down to install the turret unit. We also machined an adapter to convert the internal M24 thread of the turret to Thorlabs thread SM1. The laser beam goes into the chassis from the side port of the turret and is reflected by a dichroic mirror (Omega Optical, 555DRLP), into the microscope objective. The emissions below 560 nm, together with the 532 nm excitation, are blocked by a long-pass filter (Omega Optical, 3RD560LP) then collected by an APD (Excelitas, SPCM-AQRH-13, dark counts 170 - 250 Hz). The filters also block the 445 nm laser used for detecting the deflection of the cantilever.

To monitor and align the confocal microscope we split the collection into

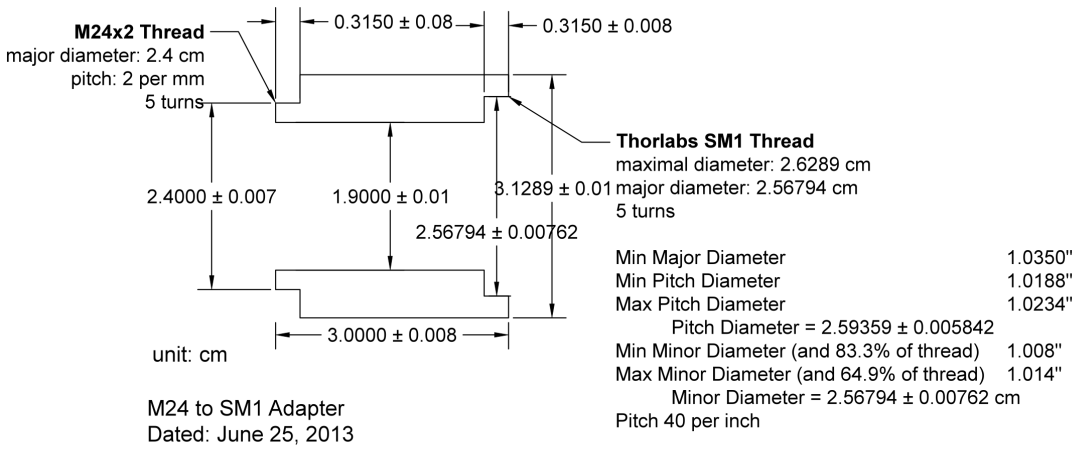

Figure 3.2: M24 Thread to Thorlab SM1 Thread Adapter

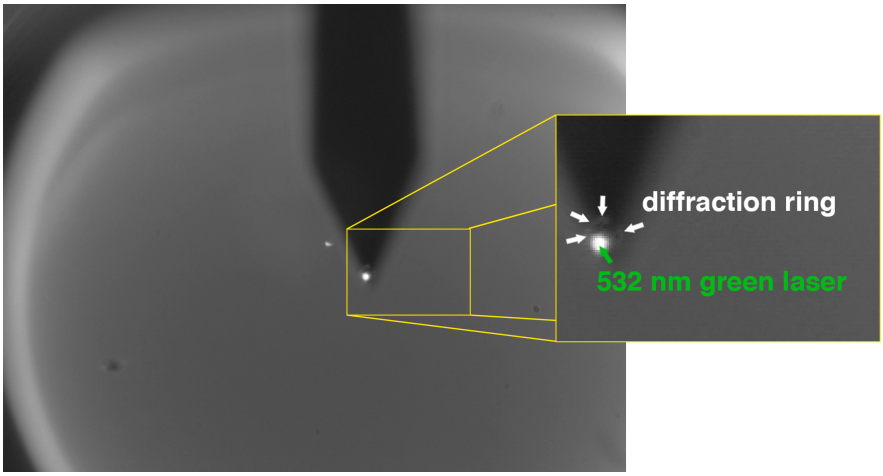

Figure 3.3: Diffraction ring of the cantilever. This screenshot shows the shadow casted by the cantilever, the bright spot due to the focused 532 nm laser, and the diffraction ring of the tip of the cantilever when the 532 nm laser effectively illuminating the tip. The screenshot is taken when there is finite separation between the tip and the top surface of the sample. The diffraction ring of the cantilever will then contract as the tip being engaged onto the top surface of the sample.

92:8 by a cube-mounted pellicle beam splitter (Thorlabs, CM1-BP108). The 8% of the emission is fed to the side port camera. Figure 3.3 is a screenshot of the side port camera taken when the tip and the focus are nearly aligned. This screenshot shows the shadow cast by the cantilever, the bright spot is due to the focused 532 nm laser, and the diffraction ring of the tip of the cantilevetr when the 532 nm is laser effectively illuminating the tip. The screenshot is taken when there is finite separation between the tip and the top surface of the sample. The diffraction ring of the cantilever will then contract as the tip engages with the top surface of the sample. It is possible to align the AFM tip to the focus of the confocal setup within 0.5 μm by carefully manually adjusting the micrometers after decoupling the stage and the head from the microscope chassis.

The Use of the Alignment Laser

We use our 635 nm alignment laser (Newport, LOA-1), which is close to the center wavelength of our collection window. The alignment laser can be coupled backward through the collection path by sending the beam into the fiber for collection (Thorlabs, M67L01).

Alignment laser is used for two reasons: (1) The collection path is more spatially confined than the excitation path, due to the f = 100 mm achromat in the collection path. Therefore the focus of the alignment laser is more sensitive, and the spot of the alignment laser is also smaller than the spot of the 532 nm laser of the excitation path. Therefore it is suggested to use the alignment laser to set the focus knob of the chassis. (2) The excitation path is not as sturdy as the collection path. It is lofty, and supported by post holder assembly, which is clamped down onto the vibration insulation stage. This would provide reasonable sta-

bility during the scans. However, the excitation path is sticking out from the chassis, unprotected, and therefore may be hit by users accidentally. Alignment laser is necessary to re-align the excitation path to the collection path.

Aligning the Tip of the Cantilever to the Focus of the Confocal Setup

The alignment of the tip of the cantilever to the focus of the 532 nm excitation beam can be done by adjusting the two micrometers which move both the AFM head and the sample stage with respect to the Olympus chassis. There are other two micrometers that only move the sample stage with respect to the AFM head and the chassis.

Crude alignment can be done with the aid of the top camera. In the top camera, before the AFM head is lowered, the spot of the green laser will be large since it is out of focus. The spot will be large enough so that the intensity gradient of the spot will be apparent, and one can find the center of the spot and move the tip to this center, which has maximal intensity. Because lowering one of the three legs of the AFM head will tilt the head, so the cantilever will move laterally. Therefore it is necessary to adjust the two micrometers repeatedly while lowering the AFM head.

The side port camera has higher magnification and smaller depth of field, so it is necessary to switch to side port camera for finer alignment. Both the spot of the excitation laser and a blurry shadow casted by the cantilever should be visible in the field of view of the side port camera when they are aligned in the top camera. The outline of the shadow will become more and more clear as the AFM head being lowered. At this point, one can engage the cantilever

onto the sample surface, retract the cantilever and aligned the tip to the spot of the excitation laser in the side port camera. When the tip and the spot of the laser are aligned, the center of the spot will appear slightly brighter, and a dim diffraction ring will be visible.

Optimization of the Correction Collar of the Objective

Our diamond or ZnO samples are fabricated on a 1 mm thick fused silica substrate (ESCO, P110040). The excitation beam passes through the substrate from beneath and illuminates our sample. To compensate for the refractive aberration introduced by the thickness of the substrate, a correction collar objective is used (Olympus, UCPLFLN20X C PLAN FLUOR 20X OBJ,CORR COL,NA0.7,WD0.8-1.8). We optimize the setting of the correction collar with respect to 635 nm alignment laser (Newport, LOA-1), which is close to the center wavelength of our collection window. Optimization is done by maximizing the sharpness of the focus and the brightness of the alignment laser sent in from the collection path. The beam of the alignment laser was sent into the collection path from a FC/PC fiber mount, and hits the sample surface, after going through the correction collar objective. The reflection at the top sample surface is collected by the objective and arrives at the camera after going through the 8:92 pellicle splitter cube. The maximal intensity of the image was recorded as a function of the position of focus knob and the data are analyzed using Mathematica.

Figure 3.4 shows several curves of intensity versus the position of the focus at different correction collar set values around 1 mm, the thickness of our substrates. The horizontal axis is the position of the focus; the vertical axis is the brightness of the brightest pixel. Each curve represents different correction

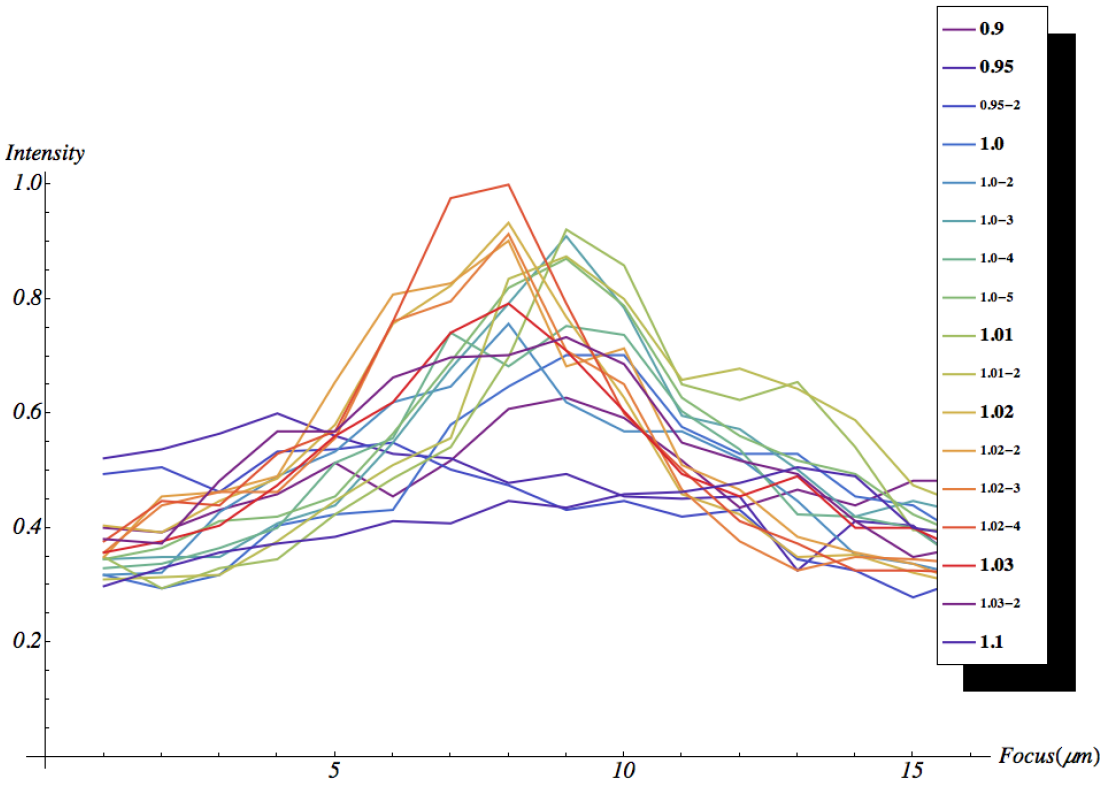

Figure 3.4: Optimization of the correction collar of the objective. The horizontal axis is the position of the focus, and the vertical the brightness of the brightest pixel. Each curve represents different correction collar setting, in mm. The optimization is done by minimizing the sharpness of the focus and maximize the brightness of the alignment laser image in camera. The beam of the alignment laser was sent into the collection path from FC/PC fiber mount, hitting the top sample surface, after going through the correction collar objective, and the reflection at the top sample surface is collected by the objective and arrives at the camera after going through the 8:92 pellicle splitter cube. The maximal intensity of the image was recorded and the data are analyzed using Mathematica.

collar setting value (in mm). Due to the mode hoping of the alignment laser, captures at same correction collar settings are repeated. Different captures are denoted by the number after dashes.

Acquisition of the Pulses from the APD

The APD outputs 1 pulse (~2.5V square pulse, with duration ~ 20 ns) per photon detected on average, which has to be counted and fed in to the Asylum scanning controller (Asylum, ARC2 Controller). An additional extended digital interface module (EDIM) of Asylum is installed to perform the task. The official Asylum ARC software (Version 120804 + 1223) is written in C and integrated onto commercial software Igor Pro by WaveMetrics. After setting up an additional channel for counts of pulses generated by APD, the default count per pixel information is displayed side-by-side with the channels for height, phase, amplitude, deflection, etc, from AFM head.

Because units such as counts per-second or kilo-counts per second are the actual measure of photoluminescence intensity, we added a function to Asylum ARC software to perform the conversion automatically. The scanning parameters that can be specified in the ARC software are in points per line, and scanning line rate. Note that in this model of AFM, the actual scanning range is 1.25 times larger than the specified range, and also that the head would perform a trace and a retrace for each line scan, so the conversion requires an additional 2.5 factor in order to return correct counts per second. Altogether, we have

$$counts/second = 1.25 \times 2 \times line\ rate \times points\ per\ line \times counts/pixel \tag{3.1}$$

The resulting counts per second is then compared by an independent time correlated single photon counting (TCSPC) module (Becker & Hickl, SPC-130). The

function is included in Appendix A. The photoluminescence intensity versus time can also be captured through the Asylum ARC 2 controller software by calling the built-in `xSetInWave` function, after a proper channel has been specified. The commands are included in Appendix B.

3.2 Preliminary Images

To test and calibrate the setup, we use spin-coated nanodiamond on patterned glass slides. The substrate is a typical glass microscope slide (Fisherbrand, plain microscope slide, 12-549-3). It turned out that the glass microscope slide gives a bright background in the confocal setup with level around 20 kc/s, as compared with 10-50 kc/s, the range of the photoluminescence intensity of isolated defects we have observed in our setup at comparable excitation power. We later switched to fused silica glass slide (ESCO, P110040). They have a background level less than 1 kc/s. The patterning is done using buffered oxide etch (BOE).

The solution of nanodiamond is purchased from Van Moppe (DiaScience-75), and further diluted by volume to a ratio of 7:57, and spin coated at 1500 rpm. Figure 3.6 (a) is an photo of the patterned microscope slide spin-coated with nanodiamond, loaded on the sample stage. There are 5×7 square patterns, and there are 47×47 smaller squares in each of the squares. Figure 3.6 (b) shows a screen capture of the top camera. The green spot is the 532 nm laser for excitation, aligned to the cantilever. The smaller squares are also visible.

Figure 3.6 shows a series of photoluminescence images of the block no. 47 and an AFM image of the spin-coated nanodiamond sample on a glass microscope slide substrate. Figure 3.6 (a) is a photoluminescence image of the block

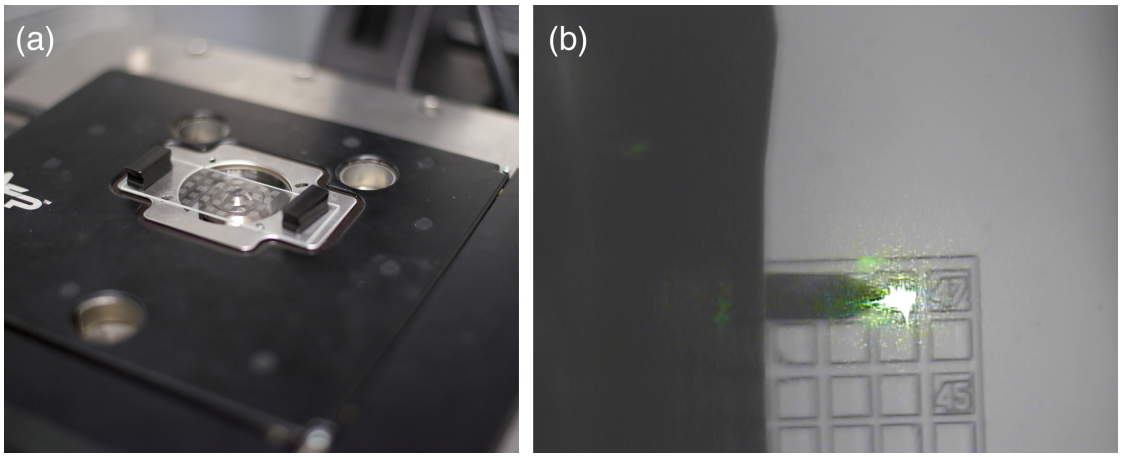

Figure 3.5: (a) An photo of the patterned microscope slide spin-coated with nanodiamond, loaded on the sample stage. There are 5 × 7 square patterns, and there are 47 × 47 smaller squares in each of the squares. (b) A screen capture of the top camera. The green spot is the 532 nm laser for excitation, aligned to the cantilever. The smaller squares are also visible.

no. 47. The backround ~20 kc/s is from the glass microscope slide substrate. The outline of the number 47 is visible. The scan size is 80 μm× 80 μm. Figure 3.6 (b) is a zoomed in image of a smaller region of block no. 47, close to one edge of the trench of 7, marked by a yellow square in (a). The scan size is approximately 8 μm× 8 μm. Figure 3.6 (c) is a further zoomed in image of a subregion of image (b), marked by a green square in (b), with (d) a corresponding AFM image of the same region. Recognizable features across the photoluminescence and the AFM images are marked by circles of different colors. The full width at half maximum of the smaller brigh spots in the fluorescence image (c) is approximately 0.6 μm. (c) and (d) suggest that the alignment of the tip of the cantilever and the confocal setup is within the resolution of the confocal setup.

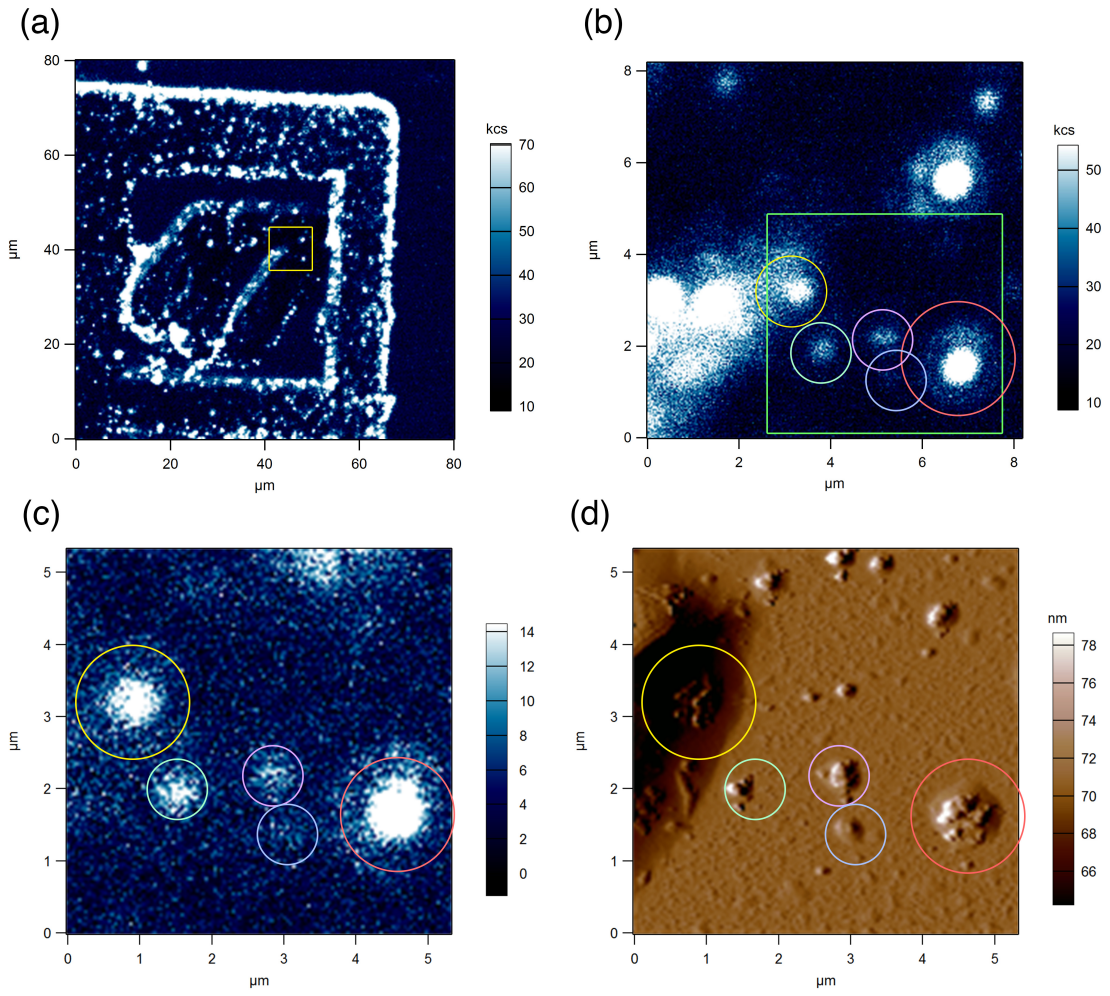

Figure 3.6: A series of photoluminescence images of the block no. 47 with an AFM image. (a) is a photoluminescence image of the block no. 47. (b) is a zoomed in image of a smaller region of block no. 47, marked by a yellow square in (a). (c) is a further zoomed in image of a subregion of image (b), marked by a green square in (b), with (d) a corresponding AFM image of the same region. Recognizable features across the photoluminescence and the AFM images are marked by circles of different colors.

CHAPTER 4

STUDY OF LOCAL TOPOGRAPHY AND PERTURBATION OF DEFECTS

In this chapter, I will describe two proposed studies on isolated defects in ZnO that would utilize the confocal setup discussed in the previous chapter: investigating local topography of the defects and optical response of the defects to an external electric field being applied across, or in the vicinity of the defects. I will also summarize the current status of the two proposed studies and future work.

4.1 Local Topography of the Defects

The first proposed study is attempting to correlate the location of isolated defects with respect to the topography. For example, would we be able to locate the defects that we have seen in fluorescence images in the AFM images such as figure 2.3. Futhremore, the widely distributed lifetimes $\tau_{|2\rangle}$ and $\tau_{|3\rangle}$, spectral peaks of different wavelengths, and widely varied photoluminescence intensity and photodyanmics that we have seen in Chapter 2 may or may not be the intrinsic properties of the defects. These could be a manifestation of unrelaxed strain around the defects, different orientations, for instance. Grain boundaries, interior regions of the grains, intergranular regions may have different local strain. Grain boundary defects, which are a distinct group from point defects, play an important role in the properties of bulk material [102,103], and affect the formation of point defects. For example, it has been reported that grain boundary in ZnO can be a sink of native point defects [104]. Due to greater freedom for relaxation, the formation energy of intrinsic point defects such as zinc vacancy V_{Zn}, and oxygen interstitials O_i, are lowered at the grain boundary and are more

likely be present.

A successful correlation of positions of defects with respect to the grains could potentially narrow down or rule out possible identities of the defect species. On the other hand, grain boundaries have local strain that is different from the interior of the grain. Therefore, correlating defects locations would enable grouping defects by their location in the grains, and possibly accounting for our observation of defect-to-defect variability among the defects. The actual correlation might be challenging because the size of the grains may be significantly smaller than the alignment of cantilever tip to the focus of excitation laser. For examples, the size of the grains in figure 2.3 are on the order of 10 nm, while the resolution of the confocal setup is on the order 100 nm.

As a first step, we have grown a 60-nm ZnO sputtered film on a patterned fused-silica microscope slide, following procedures described in section 2.2. However, we have not successfully isolated defects in this sample.

4.2 Electric Force Microscopy

A second proposed study on defects in ZnO is the optical response of the defects to an external electric field being applied across, or in the vicinity of the defects. The applied field may, for instance, change the lifetimes $\tau_{|2\rangle}$ and $\tau_{|3\rangle}$, shift the spectral peaks, or photoluminescence intensity. This experiment can be done by carefully situating the tip in the vicinity of the defect, then apply voltage between the platinum coated tip of the cantilever (Olympus, OMCL-AC240TM) and a conductive layer beneath the ZnO sample layer. The ZnO can be conductive under proper doping conditions, and a resistivity of $4.5 \times 10^{-6} \Omega \cdot m$ of has

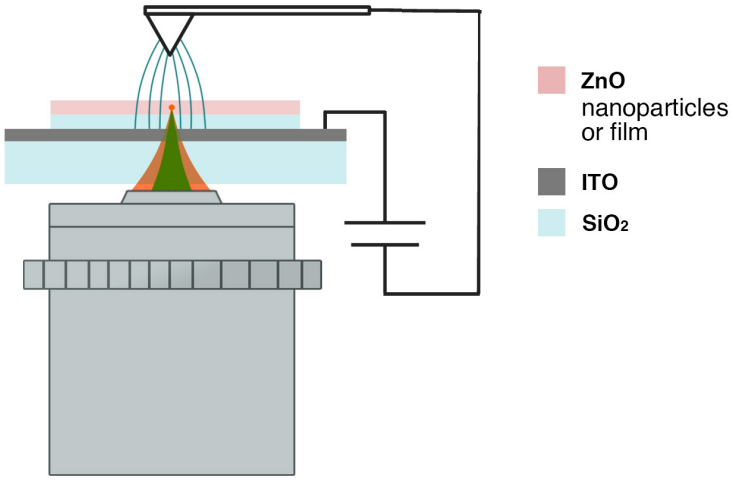

Figure 4.1: The design of our sample for electrostatic force microscopy.

been reached [105].

Figure 4.1 shows the design of our sample for electrostatic force microscopy. Our confocal-AFM setup illuminates the sample from beneath, so every additional layer except the ZnO has to be transparent to the excitation wavelength and the spectral detection window. A conductive layer is necessary for the EFM for applying a voltage. Indium tin oxide (ITO) is a convenient conductive transparent oxide and it is easy to deposit via sputtering techniques [106, 107]. Between the ITO layer and the ZnO layer, a silicon dioxide layer is inserted to provide spacing enought to bring the ZnO layer out of the near field of the conductive ITO layer in order to avoid unwanted quenching of the photoluminescence [108] or suppression of possible charged states of the defects.

The silicon dioxide layer is sputtered by RF-sputtering using a silicon dioxide target. The chamber is pumped to base pressure 3.6×10^{-6} Torr. Then argon is directed to the chamber with partial pressure 1 mTorr. The sputtering process

is done at room temperature. The thickness of deposition is monitored by doing growth with a crystal oscillator and characterized by contact profilometry. In a separate deposition for developing this recipe, the deposited 37.3 nm SiO_2 layer does not provide background with more then 1 kc/s.

The ITO is to be sputtered using the Kurt J. Lesker PVD75 sputter system, configured for ITO deposition at Cornell NanoScale Science and Technology Facility (CNF). The uniformity of the sputtered ITO increases as the sputter temperature increases [109] and the conductivity increase with the thickness in general. The transparency increases with the partial pressure of the oxygen but the conductivity of the ITO film to drop [109,110].

4.3 Conclusion and Other Future Works

We have observed isolated ZnO defects in both ZnO nanoparticle samples and sputtered films. These defects share similarities that include absorption of 532 nm and a red single-photon fluorescence emission. We have observed widely distributed excited state lifetimes $\tau_{|2\rangle}$ in the range 1-13 ns and metastable state lifetimes $\tau_{|3\rangle}$ in the range 40-300 ns. We have also observed non-classical emission with $g^{(2)}(\tau) \sim 0.5$ in Al-doped sputtered film sample. That may either be single or a small number of defects. Fluorescence blinking with dwell times of different timescales are also discussed.

I also modified an Olympus optical microscope chassis to enable co-aligned confocal microscopy integrated with a commercial AFM to investigate local topography of nanoparticles and films possessing single fluorescent defects. We have also been working to fabricate samples to monitor the optical response of

the defects in a local applied external field.

APPENDIX A

CONVERSION OF COUNTS PER PIXEL TO KILO-COUNTS PER SECOND IN ASYLUM ARC SOFTWARE

This function generates a new set of photoluminescence intensity data with unit kilo-counts per second (kc/s) from the photoluminescence intensity data with unit counts per pixel. The units such as counts per second or kilo-counts per second are the actual measure of photoluminescence intensity, so we added this function to Asylum ARC software to perform the conversion. The scanning parameters that can be specified in the ARC software are in points per line, and scanning line rate. Note that in this model of AFM (Asylum, MFP-3D), the actual scanning range is 1.25 times larger than the specified range. Note also that the piezo stage performs a trace and a retrace for each line scan, so the conversion requires an additional factor of 2. Altogether, we have

$$counts/second = 1.25 \times 2 \times line\ rate \times points\ per\ line \times counts/pixel \tag{A.1}$$

The resulting counts per second was then compared by an independent time correlated single photon counting (TCSPC) module (Becker & Hickl, SPC-130).

This function is based on the function `CalcPhaseFromIQ`, which can be found in the procedure file `XCalculated.ipf`, under `Procedure Windows` of `Windows` on the menu bar. The function was then corrected by Deron Walters at Asylum, and appended to `UserCalculated.ipf`. The `UserCalculated.ipf` is one of the procedure files that will not be altered by updates of the software. It is also the recommended location to append user-defined functions. In general, user defined functions will be loaded automatically once the program is launched, and can be accessed through the Master

Channel Panel. The user defined functions are accessible as options for channel 7 and channel 8 only. For this function we added for unit conversion, it is also necessary to assign a channel for `Counts`, since the this function generates the kilo-counts per second channel basing on the data from the original count channel.

Here I include the code which is appended to `UserCalculated.ipf`:

```
Function CalcCountsPerSec(RowIndex,ColIndex)
Variable RowIndex, ColIndex

Variable IsImage = ColIndex >= 0
String DataFolder = ""



DataFolder = GetDF("Variables")
Wave MVW = $DataFolder+"MasterVariablesWave"
Wave FVW = $DataFolder+"ForceVariablesWave"

if (IsImage)
DataFolder = "root:Packages:MFP3D:Main:"
else
DataFolder = "root:Packages:MFP3D:Force:"
ColIndex = 0
endif
String SavedDataFolder = GetDataFolder(1)
SetDataFolder(DataFolder)
```

```
if (IsImage) //Images
Wave Count = CountWave
else                //Force curves
Wave Count = Count
endif


Variable PointsPerSec
if (IsImage) //Images
//in images, points per sec derives from scan rate
Variable ScanRate = MVW[%ScanRate][%Value]
Variable ScanPoints = MVW[%ScanPoints][%Value]
PointsPerSec = 2.5*ScanRate*ScanPoints/1000
        //To display in kc/s
else //ForceCurves
//in force curves, points per sec is set directly
PointsPerSec = FVW[%NumPtsPerSec][%Value]
endif
Variable TimePerPoint = 1/PointsPerSec

SetDataFolder(SavedDataFolder)

Variable output = Count[RowIndex][ColIndex]/TimePerPoint
return(output)
```

```
End //CalcCountsperSec
```

APPENDIX B

CAPTURING COUNTS VS TIME IN ASYLUM ARC SOFTWARE

This set of commands are based on the official software tutorial of the Asylum ARC software then corrected by Deron Walters at Asylum. These commands can be typed in the command window of the software.

To setup a new capture:

```
Make/N =80 input
print td_StopInWaveBank(1)
print td_xSetInWave(1,"2,2","Count", input,
"print\"Done!\"",6250)
print td_WS("Event.2","Once")
//This will start the capture event
```

This will collect 80 data points. 6250 the duration of a time bin, in multiples of 20 μs. Therefore the duration of a bin for this case is $6250 \times 20 \times 10^{-6} = 0.125$ seconds. The overall duration is

$$80 \times 20 \times 10^{-6} \times 6250 = 10\,(sec) \tag{B.1}$$

To perform another capture. It is necessary to stop any ongoing task using the same data bank. This can be done by typing the following command:

```
print td_stop() //Command to stop the event
```

To display the data just acquired:

```
display input // Open up a window to display
```

To refresh the display window:

```
input[0]+=0
//To Refresh the displayed image after a new capture.
```

BIBLIOGRAPHY

[1] D. A. Drabold and Stefan K. Estreicher. *Theory of defects in semiconductors*. Springer, 2007.

[2] C. Santori, D. Fattal, and Y. Yamamoto. *Single-photon Devices and Applications*. John Wiley & Sons, 2010.

[3] P. Maletinsky, S. Hong, M. S. Grinolds, B. Hausmann, M. D. Lukin, R. L. Walsworth, M. Loncar, and A. Yacoby. A robust scanning diamond sensor for nanoscale imaging with single nitrogen-vacancy centres. *Nat Nanotechnol*, 7(5):320–4, 2012.

[4] M. W. Doherty T. Nbauer F. Rempp G. Balasubramanian T. Wolf F. Reinhard L. C. L. Hollenberg F. Jelezko F. Dolde, H. Fedder. Electric-field sensing using single diamond spins. *Nature Physics*, (6):459463, 2011.

[5] Romana Schirhagl, Kevin Chang, Michael Loretz, and Christian L. Degen. Nitrogen-vacancy centers in diamond: Nanoscale sensors for physics and biology. *Annual Review of Physical Chemistry*, 65(1):83–105, 2014. PMID: 24274702.

[6] V. V. Dobrovitski, G. D. Fuchs, A. L. Falk, C. Santori, and D. D. Awschalom. Quantum control over single spins in diamond. *Annual Review of Condensed Matter Physics*, 4(1):23–50, 2013.

[7] Richard P. Feynman. Simulating physics with computers. *International Journal of Theoretical Physics*, 21(6-7):467–488, 1982.

[8] Andreas Trabesinger. Quantum simulation. *Nature Physics*, (4):263263, 2012.

[9] Colin P. Williams. *Quantum Universality, Computability, & Complexity*. Springer London, 2011.

[10] P. Shor. Polynomial-time algorithms for prime factorization and discrete logarithms on a quantum computer. *SIAM Journal on Computing*, 26(5):1484–1509, 1997.

[11] Pavel Pudlk. *The Complexity of Computations*. Springer Monographs in Mathematics. Springer International Publishing, 2013.

[12] Quantum algorithms. In *Quantum Information*, pages 219–229. Springer New York, 2007.

[13] Lov K. Grover. *A Fast Quantum Mechanical Algorithm for Database Search*. STOC '96. ACM, New York, NY, USA, 1996.

[14] D. R. Simon. *On the power of quantum computation*. Nov 1994.

[15] David Deutsch and Richard Jozsa. Rapid solution of problems by quantum computation. *Proceedings of the Royal Society of London. Series A: Mathematical and Physical Sciences*, 439(1907):553–558, 1992.

[16] W. K. Wootters and W. H. Zurek. A single quantum cannot be cloned. *Nature*, (5886):802803, 1982.

[17] J. Ignacio Cirac and Peter Zoller. Goals and opportunities in quantum simulation. *Nature Physics*, (4):264266, 2012.

[18] T. Duty, D. Gunnarsson, K. Bladh, and P. Delsing. Coherent dynamics of a josephson charge qubit. *Phys. Rev. B*, 69:140503, Apr 2004.

[19] I. Chiorescu, Y. Nakamura, C. J. P. M. Harmans, and J. E. Mooij. Coherent quantum dynamics of a superconducting flux qubit. *Science*, 299(5614):1869–1871, 2003.

[20] M. H. Devoret, A. Wallraff, and J. M. Martinis. Superconducting Qubits: A Short Review. *e-print arXiv:cond-mat/0411174*, November 2004.

[21] J. T. Glueckert D. Porras T. Schaetz A. Friedenauer, H. Schmitz. Simulating a quantum magnet with trapped ions. *Nature Physics*, (10):757761, 2008.

[22] S. Olmschenk K. C. Younge D. N. Matsukevich L.-M. Duan C. Monroe D. L. Moehring, P. Maunz. Entanglement of single-atom quantum bits at a distance. *Nature*, (7158):6871, 2007.

[23] T. Schaetz M. D. Barrett R. B. Blakestad J. Britton-W. M. Itano J. D. Jost E. Knill C. Langer J. Chiaverini, D. Leibfried. Realization of quantum error correction. *Nature*, (7017):602605, 2004.

[24] Christian F. Roos, Mark Riebe, Hartmut Hffner, Wolfgang Hnsel, Jan Benhelm, Gavin P. T. Lancaster, Christoph Becher, Ferdinand Schmidt-Kaler,

and Rainer Blatt. Control and measurement of three-qubit entangled states. *Science*, 304(5676):1478–1480, 2004.

[25] Daniel Loss Guido Burkard Bjrn Trauzettel, Denis V. Bulaev. Spin qubits in graphene quantum dots. *Nature Physics*, (3):192196, 2007.

[26] Erik Nielsen, Edwin Barnes, J. P. Kestner, and S. Das Sarma. Six-electron semiconductor double quantum dot qubits. *Phys. Rev. B*, 88:195131, Nov 2013.

[27] S. Zaiser M. Jamali T. Schulte-Herbrggen H. Abe T. Ohshima J. Isoya J. F. Du P. Neumann G. Waldherr, Y. Wang. Quantum error correction in a solid-state hybrid spin register. *Nature*, (7487):204207, 2014.

[28] D. G. Cory, M. D. Price, W. Maas, E. Knill, R. Laflamme, W. H. Zurek, T. F. Havel, and S. S. Somaroo. Experimental quantum error correction. *Phys. Rev. Lett.*, 81:2152–2155, Sep 1998.

[29] E. Knill, R. Laflamme, R. Martinez, and C. Negrevergne. Benchmarking quantum computers: The five-qubit error correcting code. *Phys. Rev. Lett.*, 86:5811–5814, Jun 2001.

[30] S. E. Nigg L. Sun-L. Frunzio S. M. Girvin R. J. Schoelkopf M. D. Reed, L. DiCarlo. Realization of three-qubit quantum error correction with superconducting circuits. *Nature*, (7385):382385, 2012.

[31] Philipp Schindler, Julio T. Barreiro, Thomas Monz, Volckmar Nebendahl, Daniel Nigg, Michael Chwalla, Markus Hennrich, and Rainer Blatt. Experimental repetitive quantum error correction. *Science*, 332(6033):1059–1061, 2011.

[32] Osama Moussa, Jonathan Baugh, Colm A. Ryan, and Raymond Laflamme. Demonstration of sufficient control for two rounds of quantum error correction in a solid state ensemble quantum information processor. *Phys. Rev. Lett.*, 107:160501, Oct 2011.

[33] J. S. Hodges S. Hong J. M. Taylor P. Cappellaro L. Jiang M. V. Gurudev Dutt E. Togan A. S. Zibrov J. R. Maze, P. L. Stanwix. Nanoscale magnetic sensing with an individual electronic spin in diamond. *Nature*, (7213):644647, 2008.

[34] Gopalakrishnan Balasubramanian, I. Y. Chan, Roman Kolesov, Mohannad

Al-Hmoud, Julia Tisler, Chang Shin, Changdong Kim, Aleksander Wojcik, Philip R. Hemmer, and Anke Krueger. Nanoscale imaging magnetometry with diamond spins under ambient conditions. *Nature*, (7213):648651, 2008.

[35] P. Neumann, I. Jakobi, F. Dolde, C. Burk, R. Reuter, G. Waldherr, J. Honert, T. Wolf, A. Brunner, J. H. Shim, D. Suter, H. Sumiya, J. Isoya, and J. Wrachtrup. High-precision nanoscale temperature sensing using single defects in diamond. *Nano Letters*, 13(6):2738–2742, 2013.

[36] A. M. Zaitsev. Vibronic spectra of impurity-related optical centers in diamond. *Phys. Rev. B*, 61:12909–12922, May 2000.

[37] Kai-Mei C. Fu, Charles Santori, Paul E. Barclay, Lachlan J. Rogers, Neil B. Manson, and Raymond G. Beausoleil. Observation of the dynamic Jahn-Teller effect in the excited states of nitrogen-vacancy centers in diamond. *Physical Review Letters*, 103(25), 2009.

[38] Daniel Twitchen Matthew Markham Roman Kolesov Norikazu Mizuochi Junichi Isoya Jocelyn Achard Johannes Beck Julia Tissler Gopalakrishnan Balasubramanian, Philipp Neumann. Ultralong spin coherence time in isotopically engineered diamond. *Nature Materials*, (5):383387, 2009.

[39] A. Jarmola D. Budker R.L. Walsworth N. Bar-Gill, L.M. Pham. Solid-state electronic spin coherence time approaching one second. *Nature Communications*, page 1743, 2013.

[40] Lucio Robledo Hannes Bernien Matthew Markham Daniel J. Twitchen Ronald Hanson Wolfgang Pfaff, Tim H. Taminiau. Demonstration of entanglement-by-measurement of solid-state qubits. *Nature Physics*, (1):2933, 2012.

[41] Matthias Leifgen, Tim Schrder, Friedemann Gdeke, Robert Riemann, Valentin Mtillon, Elke Neu, Christian Hepp, Carsten Arend, Christoph Becher, Kristian Lauritsen, and Oliver Benson. Evaluation of nitrogen- and silicon-vacancy defect centres as single photon sources in quantum key distribution. *New Journal of Physics*, 16(2):023021, 2014.

[42] F. Dolde, I. Jakobi, B. Naydenov, N. Zhao, S. Pezzagna, C. Trautmann, J. Meijer, P. Neumann, F. Jelezko, and J. Wrachtrup. Room-temperature entanglement between single defect spins in diamond. *Nature Physics*, (3):139143, 2013.

[43] H. Bernien, B. Hensen, W. Pfaff, G. Koolstra, M. S. Blok, L. Robledo, T. H. Taminiau, M. Markham, D. J. Twitchen, and L. Childress. Heralded entanglement between solid-state qubits separated by three metres. *Nature*, (7447):8690, 2013.

[44] P. V Klimov, A. L Falk, B. B Buckley, and D. D Awschalom. Electrically driven spin resonance in silicon carbide color centers. *Physical Review Letters*, 112(8), 2014.

[45] W. F. Koehl, B. B. Buckley, F. J. Heremans, G. Calusine, and D. D. Awschalom. Room temperature coherent control of defect spin qubits in silicon carbide. *Nature*, 479(7371):84–U108, 2011.

[46] Y. Tu, Z. Tang, X. G. Zhao, Y. Chen, Z. Q. Zhu, J. H. Chu, and J. C. Fang. A paramagnetic neutral VAlON center in wurtzite AlN for spin qubit application. *Applied Physics Letters*, 103(7):072103, 2013.

[47] Xiaopeng Wang, Mingwen Zhao, Zhenhai Wang, Xiujie He, Yan Xi, and Shishen Yan. Spin-polarization of VGaON center in GaN and its application in spin qubit. *Applied Physics Letters*, 100(19):192401, 2012.

[48] Anthony J. Morfa, Brant C. Gibson, Matthias Karg, Timothy J. Karle, Andrew D. Greentree, Paul Mulvaney, and Snjezana Tomljenovic-Hanic. Single-photon emission and quantum characterization of zinc oxide defects. *Nano Letters*, 12(2):949–954, 2012.

[49] Ü. Özgür, Y. I. Alivov, C. Liu, A. Teke, M. A. Reshchikov, S. Doğan, V. Avrutin, S.-J. Cho, and H. Morkoç. A comprehensive review of ZnO materials and devices. *Journal of Applied Physics*, 98(4):041301, August 2005.

[50] J. C. Fan, K. M. Sreekanth, Z. Xie, S. L. Chang, and K. V. Rao. p-type ZnO materials: Theory, growth, properties and devices. *Progress in Materials Science*, 58(6):874–985, 2013.

[51] Klaus Ellmer. Transparent conductive zinc oxide and its derivatives. In David S. Ginley, editor, *Handbook of Transparent Conductors*, pages 193–263. Springer US, 2011.

[52] C. Jagadish and S.J. Pearton. *Zinc Oxide Bulk, Thin Films and Nanostructures: Processing, Properties, and Applications*. Elsevier Science, 2011.

[53] Maria Dinescu and P. Verardi. ZnO thin film deposition by laser ablation of zn target in oxygen reactive atmosphere. *Applied Surface Science*, 106(0):149 – 153, 1996. Proceedings of the Second International Conference on Photo-Excited Processes and Applications.

[54] A. El-Shaer, A. Che Mofor, A. Bakin, M. Kreye, and A. Waag. High-quality ZnO layers grown by MBE on sapphire. *Superlattices and Microstructures*, 38(46):265 – 271, 2005.

[55] E. M. Kaidashev, M. Lorenz, H. von Wenckstern, A. Rahm, H.-C. Semmelhack, K.-H. Han, G. Benndorf, C. Bundesmann, H. Hochmuth, and M. Grundmann. High electron mobility of epitaxial ZnO thin films on c-plane sapphire grown by multistep pulsed-laser deposition. *Applied Physics Letters*, 82(22), 2003.

[56] Anderson Janotti and Chris G Van de Walle. Fundamentals of zinc oxide as a semiconductor. *Reports on Progress in Physics*, 72(12):126501, 2009.

[57] Tadatsugu Minami, Hidehito Nanto, and Shinzo Takata. Highly conductive and transparent aluminum doped zinc oxide thin films prepared by rf magnetron sputtering. *Japanese Journal of Applied Physics*, 23(5A):L280, 1984.

[58] T. Minami, H. Nanto, S. Shooji, and S. Takata. The stability of zinc oxide transparent electrodes fabricated by r.f. magnetron sputtering. *Thin Solid Films*, 111(2):167 – 174, 1984.

[59] Xiang Yang Kong and Zhong Lin Wang. Spontaneous polarization-induced nanohelixes, nanosprings, and nanorings of piezoelectric nanobelts. *Nano Letters*, 3(12):1625–1631, 2003.

[60] Yong-Seok Choi, Jang-Won Kang, Dae-Kue Hwang, and Seong-Ju Park. Recent advances in ZnO-based light-emitting diodes. *Electron Devices, IEEE Transactions on*, 57(1):26–41, Jan 2010.

[61] M. S. Dahlem M. Chiesa T. Souier M. Stefancich C. Maragliano, S. Lilliu. Quantifying charge carrier concentration in ZnO thin films by scanning kelvin probe microscopy. *Scientific Reports*, pages –, 2014.

[62] L. Hozer and D. Holland. *Semiconductor ceramics: grain boundary effects*. Ellis Horwood series: Physics. Ellis Horwood, 1994.

[63] Chris G. Van de Walle. Defect analysis and engineering in ZnO. *Physica B: Condensed Matter*, 308310(0):899 – 903, 2001. International Conference on Defects in Semiconductors.

[64] A. Janotti and C. G. Van de Walle. Native point defects in ZnO. *Physical Review B*, 76(16), 2007.

[65] Fumiyasu Oba, Shigeto R. Nishitani, Seiji Isotani, Hirohiko Adachi, and Isao Tanaka. Energetics of native defects in ZnO. *Journal of Applied Physics*, 90(2):824, 2001.

[66] Chris G. Van de Walle. Hydrogen as a cause of doping in zinc oxide. 85(5):1012–1015, 2000.

[67] C. H. Park, S. B. Zhang, and S. H. Wei. Origin of p-type doping difficulty in ZnO: The impurity perspective. *Physical Review B*, 66(7), 2002.

[68] X. J. Wang, L. S. Vlasenko, S. J. Pearton, W. M. Chen, and I. A. Buyanova. Oxygen and zinc vacancies in as-grown ZnO single crystals. *Journal of Physics D-Applied Physics*, 42(17), 2009.

[69] S. B. Orlinskii, J. Schmidt, P. G. Baranov, D. M. Hofmann, C. D. Donega, and A. Meijerink. Probing the wave function of shallow Li and Na donors in ZnO nanoparticles. *Physical Review Letters*, 92(4), 2004.

[70] M. C. Tarun, M. Z. Iqbal, and M. D. McCluskey. Nitrogen is a deep acceptor in ZnO. *Aip Advances*, 1(2), 2011.

[71] N. R. Jungwirth, Y. Y. Pai, H. S. Chang, E. R. MacQuarrie, and G. D. Fuchs. A single-molecule approach to ZnO defect studies: single photons and single defects. *e-print arXiv:1402.1773*, 2014.

[72] YounJoon Jung, Eli Barkai, and Robert J. Silbey. Current status of single-molecule spectroscopy: Theoretical aspects. *The Journal of Chemical Physics*, 117(24), 2002.

[73] Christian Kurtsiefer, Sonja Mayer, Patrick Zarda, and Harald Weinfurter. Stable solid-state source of single photons. *Phys. Rev. Lett.*, 85:290–293, Jul 2000.

[74] Th. Basché, W. E. Moerner, M. Orrit, and H. Talon. Photon antibunching

in the fluorescence of a single dye molecule trapped in a solid. *Phys. Rev. Lett.*, 69:1516–1519, Sep 1992.

[75] *Modern Optical Spectroscopy*. Springer Berlin Heidelberg, 2007.

[76] J. Enderlein. Single molecule spectroscopy: Basics and applications. In M. Hof, R. Hutterer, and V. Fidler, editors, *Fluorescence Spectroscopy in Biology*, volume 3 of *Springer Series on Fluorescence*, pages 104–130. Springer Berlin Heidelberg, 2005.

[77] Partha Pratim Mondal and Alberto Diaspro. Basics of fluorescence and photophysics. In *Fundamentals of Fluorescence Microscopy*, pages 111–134. Springer Netherlands, 2014.

[78] Andrzej Molski, Johan Hofkens, Thomas Gensch, Nol Boens, and Frans De Schryver. Theory of time-resolved single-molecule fluorescence spectroscopy. *Chemical Physics Letters*, 318(45):325 – 332, 2000.

[79] Wai-Tak Yip, Dehong Hu, Ji Yu, David A. Vanden Bout, and Paul F. Barbara. Classifying the photophysical dynamics of single- and multiple-chromophoric molecules by single molecule spectroscopy. *The Journal of Physical Chemistry A*, 102(39):7564–7575, 1998.

[80] J. Schuster, F. Cichos, and C. Borczyskowski. Blinking of single molecules in various environments. *Optics and Spectroscopy*, 98(5):712–717, 2005.

[81] W. P. Ambrose, Th. Basch, and W. E. Moerner. Detection and spectroscopy of single pentacene molecules in a pterphenyl crystal by means of fluorescence excitation. *The Journal of Chemical Physics*, 95(10), 1991.

[82] W. E. Moerner W. P. Ambrose. Fluorescence spectroscopy and spectral diffusion of single impurity molecules in a crystal. *Nature*, (6306):225227, 1991.

[83] M. Vogel, A. Gruber, J. Wrachtrup, and C. von Borczyskowski. Determination of intersystem crossing parameters via observation of quantum jumps on single molecules. *The Journal of Physical Chemistry*, 99(41):14915–14917, 1995.

[84] C. Bruchle Th. Basch, S. Kummer. Direct spectroscopic observation of quantum jumps of a single molecule. *Nature*, (6510):132134, 1995.

[85] Pedro Castrillo, Dan Hessman, Mats-Erik Pistol, Jose Antonio Prieto, Craig Pryor, and Lars Samuelson. Spectroscopy, imaging and switching behaviour of individual InP/GaInP quantum dots. *Japanese Journal of Applied Physics*, 36(Part 1, No. 6B):4188–4190, 1997.

[86] Markus Lippitz, Florian Kulzer, and Michel Orrit. Statistical evaluation of single nano-object fluorescence. *ChemPhysChem*, 6(5):770–789, 2005.

[87] Stefan W. Hell and Jan Wichmann. Breaking the diffraction resolution limit by stimulated emission: stimulated-emission-depletion fluorescence microscopy. *Opt. Lett.*, 19(11):780–782, Jun 1994.

[88] Stefan Bretschneider, Christian Eggeling, and Stefan W. Hell. Breaking the diffraction barrier in fluorescence microscopy by optical shelving. *Phys. Rev. Lett.*, 98:218103, May 2007.

[89] Stefan W. Hell. Strategy for far-field optical imaging and writing without diffraction limit. *Physics Letters A*, 326(12):140 – 145, 2004.

[90] Franz J. Giessibl. Advances in atomic force microscopy. *Rev. Mod. Phys.*, 75:949–983, Jul 2003.

[91] G. Binnig, C. F. Quate, and Ch. Gerber. Atomic force microscope. *Phys. Rev. Lett.*, 56:930–933, Mar 1986.

[92] K. M. Lang, D. A. Hite, R. W. Simmonds, R. McDermott, D. P. Pappas, and John M. Martinis. Conducting atomic force microscopy for nanoscale tunnel barrier characterization. *Review of Scientific Instruments*, 75(8), 2004.

[93] L. Zhang, T. Sakai, N. Sakuma, T. Ono, and K. Nakayama. Nanostructural conductivity and surface-potential study of low-field-emission carbon films with conductive scanning probe microscopy. *Applied Physics Letters*, 75(22), 1999.

[94] Leo Gross, Fabian Mohn, Peter Liljeroth, Jascha Repp, Franz J. Giessibl, and Gerhard Meyer. Measuring the charge state of an adatom with noncontact atomic force microscopy. *Science*, 324(5933):1428–1431, 2009.

[95] Y. Martin and H. K. Wickramasinghe. Magnetic imaging by force microscopy with 1000 angstrom resolution. *Applied Physics Letters*, 50(20), 1987.

[96] E. Schaefer-Nolte, F. Reinhard, M. Ternes, J. Wrachtrup, and K. Kern. A diamond-based scanning probe spin sensor operating at low temperature in ultra-high vacuum. *Review of Scientific Instruments*, 85(1):–, 2014.

[97] Boray Torun, Berkem Ozkaya, and Guido Grundmeier. Atomic force microscopy (AFM)-based nanografting for the study of self-assembled monolayer formation of organophosphonic acids on Al2O3 single-crystal surfaces. *Langmuir*, 28(17):6919–6927, 2012.

[98] Ricardo Garcia, Ramses V. Martinez, and Javier Martinez. Nano-chemistry and scanning probe nanolithographies. *Chem. Soc. Rev.*, 35:29–38, 2006.

[99] Shareen H. Doak, Dale Rogers, Beverley Jones, Lewis Francis, R. Steven Conlan, and Chris Wright. High-resolution imaging using a novel atomic force microscope and confocal laser scanning microscope hybrid instrument: essential sample preparation aspects. *Histochemistry and Cell Biology*, 130(5):909–916, 2008.

[100] Benjamin Harke, JenuVarghese Chacko, Heiko Haschke, Claudio Canale, and Alberto Diaspro. A novel nanoscopic tool by combining AFM with STED microscopy. *Optical Nanoscopy*, 1(1):1–6, 2012.

[101] JianQiang Yu, JingHe Yuan, XueJie Zhang, JianLi Liu, and XiaoHong Fang. Nanoscale imaging with an integrated system combining stimulated emission depletion microscope and atomic force microscope. *Chinese Science Bulletin*, 58(33):4045–4050, 2013.

[102] Louisette Priester. Defects in the grain boundary structure. In *Grain Boundaries*, volume 172 of *Springer Series in Materials Science*, pages 135–146. Springer Netherlands, 2013.

[103] Shr-Nan Bai and Tseung-Yuen Tseng. The effect of grain boundaries on the electrical properties of zinc oxide-based varistor. *Journal of Electronic Materials*, 21(11):1073–1079, 1992.

[104] H. S. Domingos, J. M. Carlsson, P. D. Bristowe, and B. Hellsing. The formation of defect complexes in a ZnO grain boundary. *Interface Science*, 12(2-3):227–234, 2004.

[105] P. Gondoni, M. Ghidelli, F. Di Fonzo, V. Russo, P. Bruno, J. Mart-Rujas, C.E. Bottani, A. Li Bassi, and C.S. Casari. Structural and functional properties of Al:ZnO thin films grown by pulsed laser deposition at room

temperature. *Thin Solid Films*, 520(14):4707 – 4711, 2012. Proceedings of the EMRS 2011 Spring Meeting Symposium D: Synthesis, Processing and Characterization of Nanoscale Multi Functional Oxide Films III.

[106] Seunghun Lee, Jong-Han Lee, Sung Ju Tark, Suyoung Choi, Chan Seok Kim, Jeong Chul Lee, Won Mok Kim, and Donghwan Kim. Effect of the low-temperature annealing on Zn-doped indium-tin-oxide films for silicon heterojunction solar cells. *Japanese Journal of Applied Physics*, 51:10NA16, 2012.

[107] Yoshihiro Akagi, Katsumi Hanamoto, Hiroyuki Suzuki, Takanori Katoh, Muneo Sasaki, Shigeru Imai, Masaru Tsudagawa, Yasuyuki Nakayama, and Hidejiro Miki. Low-resistivity highly transparent indium-tin-oxide thin films prepared at room temperature by synchrotron radiation ablation. *Japanese Journal of Applied Physics*, 38(Part 1, No. 12A):6846–6850, 1999.

[108] M. Y. Shalaginov, S. Ishii, J. Liu, J. Liu, J. Irudayaraj, A. Lagutchev, A. V. Kildishev, and V. M. Shalaev. Broadband enhancement of spontaneous emission from nitrogen-vacancy centers in nanodiamonds by hyperbolic metamaterials. *Applied Physics Letters*, 102(17):–, 2013.

[109] Hai-Ning Cui, V. Teixeira, Li-Jian Meng, R. Martins, and E. Fortunato. Influence of oxygen/argon pressure ratio on the morphology, optical and electrical properties of ITO thin films deposited at room temperature. *Vacuum*, 82(12):1507 – 1511, 2008. Selected papers presented at RIVA V-5th Iberian Vacuum Meeting RIVA-5.

[110] Xuehui Wang Yipeng Chao, Wu Tang. Properties of resistivity, reflection and absorption related to structure of ito films. *Journal of Materials Sciences and Technology*, 28(4):325, 2012.